Received XX Month, XXXX; revised XX Month, XXXX; accepted XX Month, XXXX; Date of publication XX Month, XXXX; date of current version XX Month, XXXX.

Digital Object Identifier 10.1109/XXXX.2022.1234567

Passivity-Based Tracking Control of a Planetary Rover with Robotic Arm

Kristin Lakatos[1], Dominic Lakatos, Paul Kotyczka[2] and Alexander Dietrich[1], Senior Member, IEEE

[1]German Aerospace Center (DLR), Institute of Robotics and Mechatronics, Münchener Str. 20, 82234 Weßling, Germany
[2]Technical University of Munich, TUM School of Engineering and Design, Munich Institute of Robotics and Machine Intelligence (MIRMI), Chair of Automatic Control, Boltzmannstr. 15, 85748 Garching, Germany

Corresponding author: Kristin Lakatos (email: kristin.lakatos@dlr.de).

ABSTRACT Nowadays, rovers play an important role in the exploration of our nearest celestial bodies. These planetary exploration missions include both locomotion and manipulation tasks, involving physical contact situations in an unstructured environment. The requirement of increasingly autonomous task execution promotes task-space control, particularly robust and reactive control approaches. Therefore, we propose a passivity-based whole-body tracking control law for a wheeled planetary exploration rover equipped with a robotic manipulator. The control approach achieves compliant trajectory tracking at the end effector. At the same time, a corresponding platform trajectory is computed along with the torque control law, which enables whole-body reactive behavior and obviates the need for dedicated platform trajectory planning. Moreover, an extension of the control law to the regulation of a static configuration of the end effector at the end of the trajectory is proposed. We validate the presented control approach with experiments on a prototype of a planetary exploration rover. The results show that the total tracking error at the end effector is about 2.2 times smaller using the platform velocity controller than using platform torque control.

INDEX TERMS Planetary Exploration Rover, Wheeled Robots, Mobile Manipulation, Whole-body Control, Passivity-based Control, Nonholonomic Constraints, Implicit Coordination

I. INTRODUCTION

The presence of ground-based robots on foreign planets is an important step in the exploration of our solar system. Past and recent robotic missions showcase the benefits of robotic exploration in terms of scientific analysis of our nearest celestial bodies [1]. Thereby, some planetary rovers are constructed as wheeled mobile manipulators (WMMs), consisting of a robotic manipulator mounted on a wheeled mobile base [2]. The design of a rover as a WMM enables not only visual inspection of objects of scientific interest, but also physical interaction with the environment. Examples can be the collection of geological samples, the performance of in-situ measurements, or the deployment of infrastructure devices [3].

The ability to extend the workspace of the robot by combining the degrees of freedom (DOF) of platform and arm is a peculiarity of WMMs. The resulting increased kinematic redundancy can help in task execution and enables the simultaneous execution of secondary tasks. While the combined use of platform and arm via whole-body control laws has been a topic of interest in terrestrial robotics for decades, this advantage has not been fully exploited in the context of planetary exploration yet. Instead, today's planetary exploration missions are restricted to tasks that platform and arm are able to do separately. The sequential use of the subsystems can lead to iterations with time-intensive planning steps, even for simple tasks like picking up a rock. In this case, the use of more sophisticated whole-body control strategies can save time, energy and money. Moreover, the coordinated use of all available DOF of the mobile manipulator will enable future planetary rovers to perform more ambitions tasks such as harvesting water ice on the Moon or building a lunar base camp. Thus, the research goal of this work is to propose a coordinated whole-body controller for a planetary exploration rover, enabling safe interaction with an unknown environment. Thereby, the interaction is not limited to the end effector, but also occurs at the mobile platform (at least at the wheels). A suitable control concept features both robustness w. r. t.

This work is licensed under a Creative Commons Attribution 4.0 License. For more information, see https://creativecommons.org/licenses/by/4.0/

©2026 IEEE. Personal use of this material is permitted. Permission from IEEE must be obtained for all other uses, in any current or future media, including reprinting/republishing this material for advertising or promotional purposes, creating new collective works, for resale or redistribution to servers or lists, or reuse of any copyrighted component of this work in other works. DOI: 10.1109/TFR.2026.3694402

unmodeled disturbances and a well-defined contact behavior for both platform and manipulator.

A famous example of a regulation control approach that leads to a well-defined contact behavior is impedance control [4]. Compliant interaction properties while tracking a desired trajectory can be achieved by using *passivity-based* control concepts such as [5]–[7], which feature robust closed-loop behavior in the presence of disturbances and modeling errors [8]. These control algorithms are based on the concept of shaping the kinetic and potential energy of a fully actuated mechanical system, while preserving the inherent passivity of the dynamic equations [9]. Practically, this means that the natural inertia of the robot is preserved instead of artificially shaped.

While the mentioned approaches are introduced for the control of robot arms, additional considerations must be made for the control of mobile manipulators due to the peculiarities of the mobile base. The separation of locomotion and manipulation tasks is common practice not only in planetary exploration [1], but also in the related domain of field robotics [10]. Thus, recent publications of whole-body control algorithms for WMMs often deal with robotic arms on platforms in a domestic or industrial context [11]. In [12], mobile impedance techniques are applied to robots on a holonomic platform. Ren et al. apply a passivity-based tracking control law to a holonomic mobile platform, adding a disturbance rejection term [13]. While the mentioned works control both arm and platform on torque level, they have in common that the platform features special wheels (e. g. omniwheels, powered caster wheels), which are not suitable for planetary rovers, as their applicability is limited to smooth floors.

Another class of systems that can be applied in outdoor environments is differential-drive platforms or skid-steer vehicles. This type of platform can implement a desired yaw rate by reversing the rotation of two opposite wheels, which leads to wheel slip and thus energy loss by design. Examples of whole-body torque control concepts for differential-drive WMMs are given in [14]–[16]. Recent results on whole-body control of a skid-steered mobile manipulator using model predictive control (MPC) and fuzzy logic are shown in [17]. Wang et al. present a whole-body MPC framework for mobile manipulation, which is successfully demonstrated in a door-opening and traversing scenario [18].

However, steering wheels are a predominant feature of mobile robots in planetary exploration. In that case, suitable whole-body control algorithms have to deal with nonholonomic constraints imposed by the rolling-without-slipping condition of the wheels on the ground. Several works deal with the implementation of compliant whole-body control for WMMs [19]–[23]. However, these works rely on an underlying platform velocity controller and integrate the platform via an admittance simulation, which is used to assign a desired dynamic behavior to the platform. On the one hand, this control architecture is a result of the fact that most platforms provide an interface to the low-level velocity controller. Indeed, platform velocity control can be beneficial in terms of tracking performance. On the other hand, the velocity-controlled wheel actuators are not back-drivable, which prevents active compliance of the mobile platform. The admittance simulation overrides the natural platform dynamics and can lead to stability problems with the whole-body control framework in the worst case [24]. In contrast, [25] proposed an adaptive trajectory tracking controller for a WMM with uncertainties and disturbances, controlling both the manipulator joints and all platform actuators (steering and propulsion) on torque level. While the proposed control law guarantees robustness w. r. t. external disturbances in theory, the performance is validated only in simulation.

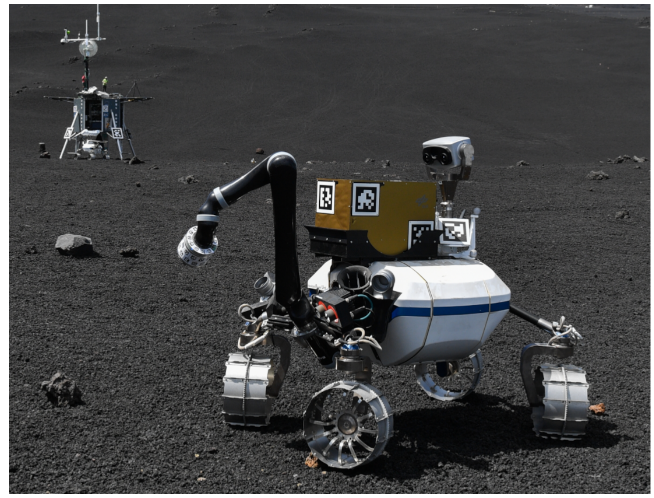

FIGURE 1: The LRU2 rover collecting stones in a space-analog campaign on Mt. Etna in Sicily/Italy in 2022 [26], [27]. The lander is visible in the background.

The scope of this work is to propose a whole-body control law for trajectory tracking with a WMM subject to nonholonomic constraints, while considering the peculiarities of a planetary exploration rover. Thereby, the steering angles are assumed to be controlled on position level, while all other actuators (wheel propulsion and arm joints) are controlled on torque level. Under these prerequisites, the control objective is to realize a compliant contact behavior for both the manipulator and the mobile base. In contrast to existing approaches, the passivity-based control law is applied to the combined system of platform and manipulator, including both the torque-controlled manipulator and the position-controlled steering actuators. As a consequence, the steering configuration of the platform is computed along with the torque control law for the remaining DOF of the robot. This beneficially implies that no separate platform trajectory planning is necessary, which is referred to as *implicit coordination*.[1] The resulting whole-body trajectory

[1]Already in [28], it is highlighted that implicit coordination control schemes are particularly suited for reactive control of mobile manipulators.

tracking controller stabilizes the combined dynamics of arm and platform to a given trajectory, either in joint space or in task space. A formal proof of exponential stability using Lyapunov theory is presented. Finally, we propose a concept to stabilize a stationary endpoint of a given task-space trajectory. Experiments with a terrestrial prototype of a planetary exploration rover (see Figure 1), with and without the emulation of planetary ground (volcanic soil), validate the approach.

The paper is organized as follows: The mathematical system model is briefly described in Section II. Next, the control approach is presented, for the joint-level case in Section III.A and for task space in Section III.B. Experimental results using a terrestrial prototype of a planetary exploration rover are described in Section IV. A discussion follows in Section V, before the paper is concluded in Section VI.

II. SYSTEM MODEL

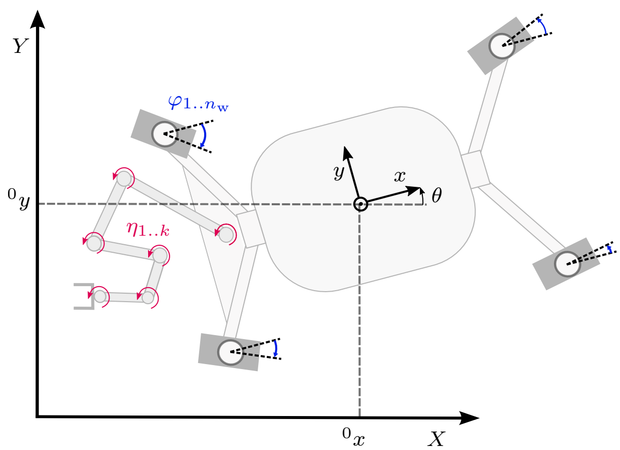

FIGURE 2: Schematic drawing of a wheeled mobile robot with $n_\mathrm{w} = 4$ steering wheels (steering angles $\boldsymbol{\varphi}$) and a robotic arm with the joint angles $\boldsymbol{\eta}$. The robot pose in the inertial frame (X, Y) is denoted by $({}^0x, {}^0y, \theta)$.

In the following, the equations of motion (EOM) for a nonholonomic mobile manipulator are derived, roughly following a common method as outlined in [29, p. 400]. Thereby, the rover is treated as a rigid body, meaning that a motion of any point on the body can be modeled as rotation around an instantaneous center of rotation (ICR).

A sketch of such a WMM featuring $n_\mathrm{w} = 4$ steering wheels and a serial robotic arm with k rotational joints is shown in Figure 2. The steering angles are denoted by $\boldsymbol{\varphi} \in \mathbb{R}^{n_\mathrm{w}}$. The 2D position of the platform in a global fixed frame (X, Y) is given by $\boldsymbol{\xi} = ({}^0x, {}^0y, \theta)$. Further, the joint angles of the robot arm are given by $\boldsymbol{\eta} \in \mathcal{Q}^k \subset \mathbb{R}^k$, where $\mathcal{Q}^k$ describes the admissible values given by the operational limits of the robot. The state of the complete robot can be consequently modeled as $\boldsymbol{q} = (\boldsymbol{\xi}^T, \boldsymbol{\eta}^T)^T \in \mathbb{R}^3 \times \mathcal{Q}^k$. The dimension of $\boldsymbol{q}$ equals $n = 3 + k$.

It is assumed that each wheel can only move in its rolling direction, no side-slip occurs. In this case, the steering wheels have to be oriented properly such that a planar motion of the platform is possible, cf. Figure 3. If this is the case, the steering configuration should be represented by a minimal set of kinematic parameters $\boldsymbol{\phi}(\boldsymbol{\varphi}) \in \mathbb{R}^r$. Thereby, r equals the number of wheels that can be oriented independently, which is commonly defined as the *degree of steerability* [30]. For the given platform design, $r = 2$ holds. From a geometrical perspective, this means that the intersection of two steering axles defines the ICR, and the remaining $n_\mathrm{w} - r$ wheels are oriented accordingly.

Then, the EOM of the rigid robot can be written as

$$\overline{\boldsymbol{M}}(\boldsymbol{q})\ddot{\boldsymbol{q}} + \overline{\boldsymbol{C}}(\boldsymbol{q}, \dot{\boldsymbol{q}})\dot{\boldsymbol{q}} + \overline{\boldsymbol{g}}(\boldsymbol{q}) = \overline{\boldsymbol{\tau}} + \overline{\boldsymbol{\tau}}_\mathrm{ext} + \boldsymbol{A}(\boldsymbol{q}, \boldsymbol{\phi})^T \boldsymbol{\lambda} \tag{1}$$

$$\boldsymbol{A}(\boldsymbol{q}, \boldsymbol{\phi})\dot{\boldsymbol{q}} = \boldsymbol{0}\,, \tag{2}$$

with the symmetric positive definite (s.p.d.) inertia matrix $\overline{\boldsymbol{M}}(\boldsymbol{q}) \in \mathbb{R}^{n \times n}$, the Coriolis/centrifugal matrix $\overline{\boldsymbol{C}}(\boldsymbol{q}, \dot{\boldsymbol{q}}) \in \mathbb{R}^{n \times n}$, and gravity terms $\overline{\boldsymbol{g}}(\boldsymbol{q}) \in \mathbb{R}^n$. It can be shown that the eigenvalues of the inertia matrix are uniformly bounded in $\boldsymbol{q}$ [31], and that $\dot{\overline{\boldsymbol{M}}} - 2\overline{\boldsymbol{C}}$ is skew-symmetric [32, p. 171]. External torques are denoted by $\overline{\boldsymbol{\tau}}_\mathrm{ext} \in \mathbb{R}^n$, and the actuation torques acting on $\boldsymbol{q}$ by $\overline{\boldsymbol{\tau}} \in \mathbb{R}^n$. The rolling-without-slipping constraints of all n_w wheels are represented by (2). The constraint matrix $\boldsymbol{A}(\boldsymbol{q}, \boldsymbol{\phi}) \in \mathbb{R}^{n_\mathrm{w} \times n}$ depends on the kinematic parameters $\boldsymbol{\phi}$. Thereby, $\mathrm{rank}(\boldsymbol{A}) = r$ holds, as r equals the number of linearly independent constraints. The constraints are non-integrable and thus nonholonomic. The corresponding constraint forces in (1) can be written as $\boldsymbol{A}(\boldsymbol{q}, \boldsymbol{\phi})^T \boldsymbol{\lambda}$, which can be easily verified by the principle of virtual work. Thereby, the Lagrangian multipliers $\boldsymbol{\lambda} \in \mathbb{R}^{n_\mathrm{w}}$ can be interpreted as reaction forces orthogonal to the feasible motion directions.

In order to eliminate the constraint forces from (1), a velocity transformation

$$\dot{\boldsymbol{q}} = \boldsymbol{S}(\boldsymbol{q}, \boldsymbol{\phi})\boldsymbol{v} \tag{3}$$

is performed. The matrix $\boldsymbol{S} \in \mathbb{R}^{n \times (n-r)}$ is chosen to represent the null space of the constraint matrix, that is, $\boldsymbol{A}(\boldsymbol{q}, \boldsymbol{\phi})\boldsymbol{S}(\boldsymbol{q}, \boldsymbol{\phi}) = \boldsymbol{0}$. Thereby, $\boldsymbol{v} \in \mathbb{R}^{n-r}$ denotes the instantaneously feasible velocities w. r. t. the steering configuration $\boldsymbol{\phi}$.

Remark 1. In general, there are different possibilities for choosing $\boldsymbol{\phi}$ and $\boldsymbol{v}$.[2] One example is to define the Cartesian coordinates of the ICR of the platform as the kinematic parameters $\boldsymbol{\phi}$, or use spherical ICR coordinates as proposed in [33]. The corresponding velocity variable is then $\boldsymbol{v} = (\omega_\mathrm{ICR}, \dot{\boldsymbol{\eta}}^T)^T$, with ω_ICR denoting the angular velocity of the platform around the ICR. We employ another parameterization, where

[2] An overview of possible parameterizations for different platform designs can be found in [30].

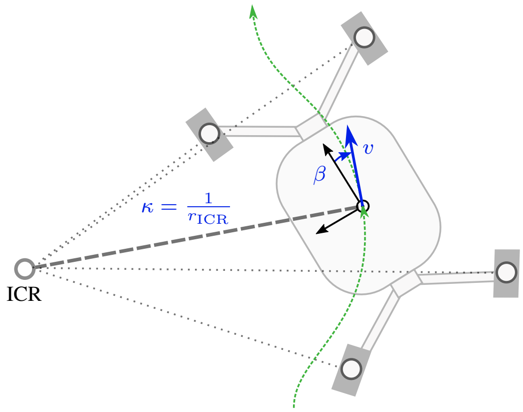

FIGURE 3: Parameterization of the steering configuration via curvature κ (inverse of the distance to the instantaneous center of rotation, r_{ICR}) and lateral driving angle β. The velocity v denotes the translational velocity tangential to the path of the platform.

$\boldsymbol{\phi}$ is chosen as the curvature κ and the lateral driving angle β. The corresponding platform velocity v is tangential to the path of the platform. The geometrical interpretation of this parameterization and its relation to the position of the ICR is sketched in Figure 3.

Remark 2. Depending on the parameterization of $\boldsymbol{\phi}$, (3) can be locally inverted to determine $\boldsymbol{\phi} \in \mathbb{R}^r$ and $\boldsymbol{v} \in \mathbb{R}^{n-r}$ from a given velocity $\dot{\boldsymbol{q}} \in \mathbb{R}^n$.

To eliminate the constraint forces $\boldsymbol{A}(\boldsymbol{q}, \boldsymbol{\phi})^T \boldsymbol{\lambda}$ from the EOM, (1)–(2) are left-multiplied by $\boldsymbol{S}(\boldsymbol{q}, \boldsymbol{\phi})^T$. This yields the *constraint-consistent dynamic equations*:

$$\boldsymbol{M}(\boldsymbol{q}, \boldsymbol{\phi})\dot{\boldsymbol{v}} + \boldsymbol{C}(\boldsymbol{q}, \boldsymbol{v}, \boldsymbol{\phi}, \dot{\boldsymbol{\phi}})\boldsymbol{v} + \boldsymbol{g}(\boldsymbol{q}, \boldsymbol{\phi}) = \boldsymbol{\tau} + \boldsymbol{\tau}_{\mathrm{ext}} \tag{4}$$

with

$$\begin{aligned} \boldsymbol{M}(\boldsymbol{q}, \boldsymbol{\phi}) &= \boldsymbol{S}^T \overline{\boldsymbol{M}} \boldsymbol{S}\,, \\ \boldsymbol{C}(\boldsymbol{q}, \boldsymbol{v}, \boldsymbol{\phi}, \dot{\boldsymbol{\phi}}) &= \boldsymbol{S}^T \overline{\boldsymbol{M}} \dot{\boldsymbol{S}} + \boldsymbol{S}^T \overline{\boldsymbol{C}} \boldsymbol{S}\,, \\ \boldsymbol{g}(\boldsymbol{q}, \boldsymbol{\phi}) &= \boldsymbol{S}^T \bar{\boldsymbol{g}}\,, \\ \boldsymbol{\tau}(\boldsymbol{q}, \boldsymbol{\phi}) &= \boldsymbol{S}^T \bar{\boldsymbol{\tau}}\,, \\ \boldsymbol{\tau}_{\mathrm{ext}}(\boldsymbol{q}, \boldsymbol{\phi}) &= \boldsymbol{S}^T \bar{\boldsymbol{\tau}}_{\mathrm{ext}}\,. \end{aligned} \tag{5}$$

For bounded $\boldsymbol{\phi}$ and $\dot{\boldsymbol{\phi}}$, it can be verified that $\boldsymbol{M}(\boldsymbol{q}, \boldsymbol{\phi})$ is s.p.d., and $\dot{\boldsymbol{M}} - 2\boldsymbol{C}$ is skew-symmetric. Note that from now on, dependencies on $\boldsymbol{q}$ and $\boldsymbol{\phi}$ and their derivatives are only written if strictly necessary for the understanding.

The external forces $\boldsymbol{\tau}_{\mathrm{ext}}$ are written as a sum

$$\boldsymbol{\tau}_{\mathrm{ext}} = \boldsymbol{\tau}_{\mathrm{wgc}} + \boldsymbol{\tau}_{\mathrm{con}}\,, \tag{6}$$

with

$$\boldsymbol{\tau}_{\mathrm{wgc}} = \begin{pmatrix} \boldsymbol{\tau}_{\mathrm{wgc,p}} \\ \boldsymbol{0} \end{pmatrix} \tag{7}$$

and $\boldsymbol{\tau}_{\mathrm{wgc,p}} \in \mathbb{R}^{3-r}$ denoting the generalized forces acting on the platform due to wheel-ground contact (such as the nominal amount of friction that occurs between wheels and ground while driving on the respective soil). The remaining external forces acting on the platform and the arm in the feasible motion direction are denoted by $\boldsymbol{\tau}_{\mathrm{con}}$ (e. g. , generalized forces that occur in contact with obstacles or a human operator). Note that joint friction forces are compensated by the low-level joint controllers.[3]

Then, the constraint-consistent EOM can be formulated in state space as

$$\dot{\boldsymbol{q}} = \boldsymbol{S}(\boldsymbol{\phi})\boldsymbol{v} \tag{8}$$

$$\boldsymbol{M}\dot{\boldsymbol{v}} + \boldsymbol{C}\boldsymbol{v} + \boldsymbol{g} = \boldsymbol{\tau} + \boldsymbol{\tau}_{\mathrm{wgc}} + \boldsymbol{\tau}_{\mathrm{con}} \tag{9}$$

where (8) will be called the *kinematic subsystem*, and (9) is the *dynamic subsystem* in the following. For the control design, the actuation torques $\boldsymbol{\tau}$ and the kinematic parameters $\boldsymbol{\phi}$ are considered as system inputs. The kinematic parameters are physically created by steering the wheels appropriately, which is conducted by an underlying position control loop.

III. Control approach and stability analysis

In the following, a trajectory tracking controller for nonholonomic mobile manipulators is introduced. The control concept includes the extension of passivity-based tracking control to the class of WMMs with nonholonomic constraints. The advantages of the passivity-based controllers are, among others, the intuitive stability analysis leading to comprehensible tuning strategies and the preservation of the natural inertia. The latter property is highly beneficial in terms of robustness in practice, see e. g. [8]. The control algorithm adopts the idea of restricting the steady-state position errors to a sliding surface and turns it into kinematic stability conditions, which generate reference values for both the torque-controlled and the position-controlled DOF (i. e., the steering configuration).

The baseline controller has been been introduced in [7] for holonomic robot arms, together with a parameter adaptation in order to deal with modeling uncertainties. In this work, we assume a perfect system model and thus exclude the parameter adaptation for the sake of clarity; however, it should be possible to extend the proposed algorithm by the respective terms if needed.

In the following, the control law is introduced and discussed in joint space. Afterwards, an extension to the task space is conducted. Thereby, a novel switching approach is developed, which makes it possible to achieve asymptotic stability of the time-dependent desired trajectory (tracking case) with a static endpoint (regulation case).

A. Joint-Level tracking controller design

Let $\boldsymbol{q}_{\mathrm{des}}(t)$, $\dot{\boldsymbol{q}}_{\mathrm{des}}(t)$, $\ddot{\boldsymbol{q}}_{\mathrm{des}}(t)$ be a given (uniformly continuous and bounded) trajectory in the joint space. The tracking error is defined as $\tilde{\boldsymbol{q}}(t) = \boldsymbol{q} - \boldsymbol{q}_{\mathrm{des}}(t)$, with the time derivatives $\dot{\tilde{\boldsymbol{q}}}(t), \ddot{\tilde{\boldsymbol{q}}}(t)$. As of now, dependencies on time will be omitted in the notation and only written if strictly necessary for the understanding.

[3]Joint friction can be compensated, for example, according to the methods presented in [34].

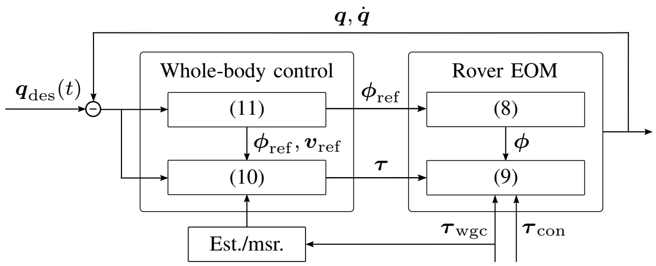

FIGURE 4: Control architecture diagram for the joint-level tracking controller.

In the following considerations, the following assumptions are made:

Assumption 1. *The desired trajectory is chosen such that the reference kinematic parameters* $\boldsymbol{\phi}_{\mathrm{ref}}$ *and their first derivatives* $\dot{\boldsymbol{\phi}}_{\mathrm{ref}}$ *are bounded.*

Assumption 2. *The low-level steering controllers are assumed to be ideal, such that* $\boldsymbol{\phi} \equiv \boldsymbol{\phi}_{\mathrm{ref}}$ *holds.*

Assumption 3. *The nominal wheel-ground interaction forces* $\boldsymbol{\tau}_{\mathrm{wgc}}$ *can be computed from known and measured quantities.*

Clearly, the validity of the assumptions depends strongly of the hardware capabilities in combination with the choice of the desired trajectory. A discussion of these aspects, in the light of experimental results, is part of Section V.

1) Control law

In order to track a trajectory in the joint space, we propose the following passivity-based control law for the dynamic subsystem (9):

$$\begin{aligned}\boldsymbol{\tau} = \boldsymbol{M}\dot{\boldsymbol{v}}_{\mathrm{ref}} + \boldsymbol{C}\boldsymbol{v}_{\mathrm{ref}} + \boldsymbol{g} - \boldsymbol{\tau}_{\mathrm{wgc}} - \boldsymbol{H}(\boldsymbol{q}, \boldsymbol{\phi}_{\mathrm{ref}})\boldsymbol{s} \\ -\boldsymbol{S}(\boldsymbol{q}, \boldsymbol{\phi}_{\mathrm{ref}})^T \boldsymbol{K}\widetilde{\boldsymbol{q}}\,,\end{aligned} \tag{10}$$

with a uniformly bounded s.p.d. damping matrix $\boldsymbol{H}(\boldsymbol{q}, \boldsymbol{\phi}_{\mathrm{ref}}) \in \mathbb{R}^{(n-r)\times(n-r)}$ and the constant diagonal p.d. stiffness matrix $\boldsymbol{K} \in \mathbb{R}^{n\times n}$. The reference velocity $\boldsymbol{v}_{\mathrm{ref}}$ and the kinematic parameters $\boldsymbol{\phi}_{\mathrm{ref}}$ are chosen as the solution of

$$\boldsymbol{S}(\boldsymbol{q}, \boldsymbol{\phi}_{\mathrm{ref}})\boldsymbol{v}_{\mathrm{ref}} = \dot{\boldsymbol{q}}_{\mathrm{des}} - \boldsymbol{\Omega}\widetilde{\boldsymbol{q}} \tag{11}$$

with the s.p.d. diagonal gain matrix $\boldsymbol{\Omega} \in \mathbb{R}^{n\times n}$,

$$\boldsymbol{s} = \boldsymbol{v} - \boldsymbol{v}_{\mathrm{ref}} \tag{12}$$

denotes the velocity error. The controller structure is shown in Figure 4.

From (8) and (12), and inserting (10) into (9), the closed-loop equations in error coordinates are derived as

$$\dot{\widetilde{\boldsymbol{q}}} = \boldsymbol{S}(\boldsymbol{q}, \boldsymbol{\phi}_{\mathrm{ref}})(\boldsymbol{s} + \boldsymbol{v}_{\mathrm{ref}}) - \dot{\boldsymbol{q}}_{\mathrm{des}} \tag{13}$$

$$\boldsymbol{M}\dot{\boldsymbol{s}} + (\boldsymbol{C} + \boldsymbol{H})\boldsymbol{s} + \boldsymbol{S}^T\boldsymbol{K}\widetilde{\boldsymbol{q}} = \boldsymbol{\tau}_{\mathrm{con}}\,. \tag{14}$$

As a consequence, the closed-loop dynamics is stabilized to the desired trajectory, as the following proposition shows. For this reason, (11) is referred to as the *kinematic stability condition* in the following.

Proposition 1.
In the case of free motion, the closed-loop error dynamics (13)–(14) *has a uniformly exponentially stable equilibrium at* $(\widetilde{\boldsymbol{q}}^*, \boldsymbol{s}^*) = (\mathbf{0}, \mathbf{0})$, *if the reference values* $\boldsymbol{\phi}_{\mathrm{ref}}, \boldsymbol{v}_{\mathrm{ref}}$ *satisfy* (11).

Proof:
The storage function $V_v : (\mathbb{R}^3 \times \mathcal{Q}^k) \times \mathbb{R}^{(n-r)} \times \mathbb{R}^+ \to \mathbb{R}$ is chosen as

$$V_v(\widetilde{\boldsymbol{q}}, \boldsymbol{s}, t) = \frac{1}{2}\boldsymbol{s}^T\boldsymbol{M}(\widetilde{\boldsymbol{q}}, \boldsymbol{\phi}, t)\boldsymbol{s} + \frac{1}{2}\widetilde{\boldsymbol{q}}^T\boldsymbol{K}\widetilde{\boldsymbol{q}}\,, \tag{15}$$

which is p.d. in $(\widetilde{\boldsymbol{q}}, \boldsymbol{s})$ for all t. Note that V_v is time-dependent, which necessitates the use of theorems for non-autonomous systems in the stability analysis. The total time derivative of (15) is

$$\begin{aligned}\dot{V}_v(\widetilde{\boldsymbol{q}}, \boldsymbol{s}, t) =& \boldsymbol{s}^T\boldsymbol{\tau}_{\mathrm{con}} - \boldsymbol{s}^T\boldsymbol{H}(\widetilde{\boldsymbol{q}}, \boldsymbol{\phi}_{\mathrm{ref}}, t)\boldsymbol{s} \\ &+ \widetilde{\boldsymbol{q}}^T\boldsymbol{K}(\boldsymbol{S}(\widetilde{\boldsymbol{q}}, \boldsymbol{\phi}_{\mathrm{ref}}, t)\boldsymbol{v}_{\mathrm{ref}} - \dot{\boldsymbol{q}}_{\mathrm{des}}(t))\,.\end{aligned} \tag{16}$$

Inserting (11) into (16) yields

$$\dot{V}_v(\widetilde{\boldsymbol{q}}, \boldsymbol{s}, t) = \boldsymbol{s}^T\boldsymbol{\tau}_{\mathrm{con}} - \boldsymbol{s}^T\boldsymbol{H}(\widetilde{\boldsymbol{q}}, \boldsymbol{\phi}_{\mathrm{ref}}, t)\boldsymbol{s} - \widetilde{\boldsymbol{q}}^T\boldsymbol{K}\boldsymbol{\Omega}\widetilde{\boldsymbol{q}}\,. \tag{17}$$

For the case of undisturbed motion (i. e., $\boldsymbol{\tau}_{\mathrm{con}} = \mathbf{0}$), the storage function $V_v(\widetilde{\boldsymbol{q}}, \boldsymbol{s}, t)$ is a strict Lyapunov function for (13)–(14) with the time derivative $\dot{V}_v$ being negative definite in $(\widetilde{\boldsymbol{q}}, \boldsymbol{s})$. In particular, this implies the boundedness of the state $(\widetilde{\boldsymbol{q}}, \boldsymbol{s})$.

Next, it can be shown that V_v is decrescent. Let $\lambda_i(\cdot)$ denote the i-th eigenvalue of a matrix. From the uniform boundedness of the eigenvalues of the inertia matrix and the min-max theorem[4] it follows that there exist time-independent lower and upper bounds for $V_v(\widetilde{\boldsymbol{q}}, \boldsymbol{s}, t)$:

$$\begin{aligned}\underline{V}_v(\widetilde{\boldsymbol{q}}, \boldsymbol{s}) = \frac{1}{2}\inf_{\boldsymbol{q},\boldsymbol{\phi}}\min_i \lambda_i(\boldsymbol{M}(\boldsymbol{q}, \boldsymbol{\phi}))\|\boldsymbol{s}\|^2 + \\ \frac{1}{2}\min_i \lambda_i(\boldsymbol{K})\|\widetilde{\boldsymbol{q}}\|^2\end{aligned} \tag{18}$$

$$\begin{aligned}\overline{V}_v(\widetilde{\boldsymbol{q}}, \boldsymbol{s}) = \frac{1}{2}\sup_{\boldsymbol{q},\boldsymbol{\phi}}\max_i \lambda_i(\boldsymbol{M}(\boldsymbol{q}, \boldsymbol{\phi}))\|\boldsymbol{s}\|^2 + \\ \frac{1}{2}\max_i \lambda_i(\boldsymbol{K})\|\widetilde{\boldsymbol{q}}\|^2\,.\end{aligned} \tag{19}$$

Further, the time derivative (17) is bounded by

$$\begin{aligned}\dot{\overline{V}}_v(\widetilde{\boldsymbol{q}}, \boldsymbol{s}) = -\inf_{\boldsymbol{q},\boldsymbol{\phi}}\min_i \lambda_i(\boldsymbol{H}(\boldsymbol{q}, \boldsymbol{\phi}))\|\boldsymbol{s}\|^2 - \\ \min_i \lambda_i(\boldsymbol{K}\boldsymbol{\Omega})\|\widetilde{\boldsymbol{q}}\|^2\,.\end{aligned} \tag{20}$$

Thus, the inequalities

$$\underline{V}_v(\widetilde{\boldsymbol{q}}, \boldsymbol{s}) \le V_v(\widetilde{\boldsymbol{q}}, \boldsymbol{s}, t) \le \overline{V}_v(\widetilde{\boldsymbol{q}}, \boldsymbol{s}) \tag{21}$$

and

$$\dot{V}_v(\widetilde{\boldsymbol{q}}, \boldsymbol{s}, t) \le \dot{\overline{V}}_v(\widetilde{\boldsymbol{q}}, \boldsymbol{s}) < 0 \tag{22}$$

hold for all $(\widetilde{\boldsymbol{q}}, \boldsymbol{s}) \neq (\mathbf{0}, \mathbf{0})$. According to the exponential stability theorem [37, p. 154, Theorem 4.10], this proves uniform exponential stability of $(\widetilde{\boldsymbol{q}}^*, \boldsymbol{s}^*) = (\mathbf{0}, \mathbf{0})$. ∎

[4]The min-max theorem follows from the Courant-Fischer theorem [35], [36] and states that $\min_i \lambda_i(\boldsymbol{B})\|\boldsymbol{z}\|^2 \le \boldsymbol{z}^T\boldsymbol{B}\boldsymbol{z} \le \max_i \lambda_i(\boldsymbol{B})\|\boldsymbol{z}\|^2 \ \forall \boldsymbol{z}$ for a s.p.d. matrix $\boldsymbol{B}$.

Remark 3. From (17), passivity of the closed-loop system (13)–(14) w. r. t. the power port $(\boldsymbol{\tau}_{\text{con}}, \boldsymbol{s})$ can be concluded immediately.

Remark 4. From (13) and (11), it follows that

$$\dot{\widetilde{\boldsymbol{q}}} = -\boldsymbol{\Omega}\widetilde{\boldsymbol{q}} + \boldsymbol{S}(\boldsymbol{q}, \phi_{\text{ref}})\boldsymbol{s}\,, \tag{23}$$

which can be interpreted as a stable dynamics of $\widetilde{\boldsymbol{q}}$ with the input $\boldsymbol{s}$. It can be concluded that the convergence of $\boldsymbol{s} \to \boldsymbol{0}$ leads to the convergence $\widetilde{\boldsymbol{q}} \to \boldsymbol{0}$ as $t \to \infty$.

Remark 5. Note that the Lyapunov function (15) is radially unbounded for $(\widetilde{\boldsymbol{q}}, \boldsymbol{s}) \in (\mathbb{R}^3 \times \mathcal{Q}^k) \times \mathbb{R}^{(n-r)}$. In this sense, the proof of stability holds globally.

2) Discussion of the controller gains

For practical use, a question of interest is how to select the controller gains. Clearly, the values of $\boldsymbol{H}, \boldsymbol{K}$, and $\boldsymbol{\Omega}$ influence both the convergence properties of the closed-loop error dynamics and the stiffness and damping characteristics of the robot in interaction with the environment. The influence of the gains, considering the interaction properties of a holonomic arm, is discussed in detail in [38]. For a holonomic system, it can be shown that the gains can be used both to parameterize the convergence rate of the tracking errors and to specify a desired contact stiffness and damping. In principle, these considerations can also be used as guidelines for the nonholonomic system at hand. However, another important aspect arises for the considered system in practice, and that is the performance of the underlying steering position controller.

From (11), it follows that the value of $\boldsymbol{\Omega}$ directly influences the effect of the tracking error on the computation of the steering configuration. Thus, selecting higher values for $\boldsymbol{\Omega}$ results in a more "sensitive" steering behavior. In order to analyze the influence of $\boldsymbol{K}$ and $\boldsymbol{H}$, the control law (10) is written in terms of the unconstrained system matrices (the transformations are given in (5)). Moreover, the derivative of (11) w. r. t. time

$$\dot{\boldsymbol{S}}\boldsymbol{v}_{\text{ref}} + \boldsymbol{S}\dot{\boldsymbol{v}}_{\text{ref}} = \ddot{\boldsymbol{q}}_{\text{des}} - \boldsymbol{\Omega}\dot{\widetilde{\boldsymbol{q}}} \tag{24}$$

is used, and $\boldsymbol{H}$ is assumed to be chosen such that it can be written as

$$\boldsymbol{H}(\boldsymbol{q}, \boldsymbol{\phi}) = \boldsymbol{S}^T \overline{\boldsymbol{H}} \boldsymbol{S}\,. \tag{25}$$

Sorting the result yields

$$\begin{aligned} \boldsymbol{\tau} &= \boldsymbol{S}^T \overline{\boldsymbol{M}} \ddot{\boldsymbol{q}}_{\text{des}} + \boldsymbol{S}^T \overline{\boldsymbol{C}} \dot{\boldsymbol{q}}_{\text{des}} + \boldsymbol{S}^T \overline{\boldsymbol{g}} - \boldsymbol{\tau}_{\text{wgc}} \\ &\quad - \boldsymbol{S}^T (\overline{\boldsymbol{M}}\boldsymbol{\Omega} + \overline{\boldsymbol{H}}\boldsymbol{\Omega})\dot{\widetilde{\boldsymbol{q}}} - \boldsymbol{S}^T (\overline{\boldsymbol{C}}\boldsymbol{\Omega} + \overline{\boldsymbol{H}}\boldsymbol{\Omega} + \boldsymbol{K})\widetilde{\boldsymbol{q}}\,. \end{aligned} \tag{26}$$

The first four terms model feed-forward action, gravity compensation, and friction compensation. The fifth term is the effective feedback of the velocity error $\dot{\widetilde{\boldsymbol{q}}}$; thus, the corresponding gain $-\boldsymbol{S}^T (\overline{\boldsymbol{M}}\boldsymbol{\Omega} + \overline{\boldsymbol{H}}\boldsymbol{\Omega})$ is called the *effective D-gain*. Accordingly, the feedback gain multiplied by the position error $\widetilde{\boldsymbol{q}}$ is referred to as the *effective P-gain*. It can be observed that both the effective P-gain and D-gain are combinations of matrices of the state space model with the gain matrices $\overline{\boldsymbol{H}}, \boldsymbol{K}$, and $\boldsymbol{\Omega}$, left-multiplied by $\boldsymbol{S}^T$. Thus, for a given $\boldsymbol{\Omega}$, the values of $\boldsymbol{K}$ and $\overline{\boldsymbol{H}}$ parameterize the convergence of the system in the direction of the instantaneously feasible velocity. In particular, the effective P-gain $\boldsymbol{K}_{\text{eff}} = -\boldsymbol{S}^T (\overline{\boldsymbol{C}}\boldsymbol{\Omega} + \overline{\boldsymbol{H}}\boldsymbol{\Omega} + \boldsymbol{K})$ models the stiffness of the closed-loop system in the direction of the instantaneously feasible motion, while the effective D-gain influences the associated damping. In this context, it can be observed that the convergence rate of the Lyapunov function (15) depends on $\boldsymbol{H}$ and the product $\boldsymbol{K}\boldsymbol{\Omega}$, see (20) and (22). This means that weighting $\boldsymbol{K}$ versus $\boldsymbol{\Omega}$ while keeping their product constant yields a constant decrease rate of the error state $(\widetilde{\boldsymbol{q}}, \boldsymbol{s})$. Thereby, the behavior of the closed-loop system can be "shifted" between the steering sensitivity (parametrized by $\boldsymbol{\Omega}$) and the parameterization of the closed-loop stiffness tangential to the trajectory, influenced by $\boldsymbol{K}$.

Summarized, a reasonable tuning strategy for the controller gains is to first choose the value for $\boldsymbol{\Omega}$, depending on the performance of the low-level steering controllers. Then, select $\boldsymbol{K}$ and $\boldsymbol{H}$ according to the desired tracking behavior along the instantaneously feasible motion direction (i. e., the perceived stiffness and damping or the convergence rate of the tracking errors).

3) Extension to kinematic platform control

In practice, most mobile platforms rather feature a kinematic control interface (based on wheel velocity controllers) than a torque interface which implements torques at the single wheels. One of the reasons for this fact is the need for complicated modeling and compensation of wheel-ground contact forces. Thus, it is worth mentioning that the control algorithm at hand can also be extended to systems without a platform torque interface. In this case, the kinematic stability conditions are solved w. r. t. the kinematic parameters ϕ_{ref} and the platform reference velocity v_{ref}, which are then implemented by the low-level platform velocity controller directly (without computing an actuation torque for the platform).

Assumption 4. *The closed-loop dynamics of the velocity-controlled platform is sufficiently fast, such that $v \simeq v_{\text{ref}}$ can be assumed.*

For proving the stability under platform velocity control, the dynamic equations of the mobile manipulator (8)–(9), as well as the kinematic stability condition (11), are written w. r. t. both platform and arm variables:

1) Kinematic subsystem (8):

$$\begin{pmatrix} \dot{\boldsymbol{\xi}} \\ \dot{\boldsymbol{\eta}} \end{pmatrix} = \begin{pmatrix} \boldsymbol{\Sigma}(\boldsymbol{q}, \phi_{\text{ref}}) & \boldsymbol{0} \\ \boldsymbol{0} & \boldsymbol{I} \end{pmatrix} \begin{pmatrix} v_{\text{ref}} \\ \dot{\boldsymbol{\eta}} \end{pmatrix}, \tag{27}$$

where $\boldsymbol{\Sigma}(\boldsymbol{q}, \boldsymbol{\phi}_{\mathrm{ref}}) \in \mathbb{R}^{3\times(3-r)}$ is the part of $\boldsymbol{S}(\boldsymbol{q}, \boldsymbol{\phi}_{\mathrm{ref}})$ acting on the platform velocity.

2) Dynamic subsystem (9):

$$\begin{pmatrix} \boldsymbol{M}_{\mathrm{p}} & \boldsymbol{M}_{\mathrm{pm}} \\ \boldsymbol{M}_{\mathrm{pm}}^T & \boldsymbol{M}_{\mathrm{m}} \end{pmatrix} \begin{pmatrix} \dot{v}_{\mathrm{ref}} \\ \ddot{\boldsymbol{\eta}} \end{pmatrix} + \begin{pmatrix} \boldsymbol{C}_{\mathrm{p}} & \boldsymbol{C}_{\mathrm{pm}} \\ \boldsymbol{C}_{\mathrm{mp}} & \boldsymbol{C}_{\mathrm{m}} \end{pmatrix} \begin{pmatrix} v_{\mathrm{ref}} \\ \dot{\boldsymbol{\eta}} \end{pmatrix} + \begin{pmatrix} \boldsymbol{g}_{\mathrm{p}} \\ \boldsymbol{g}_{\mathrm{m}} \end{pmatrix} = \begin{pmatrix} \boldsymbol{\tau}_{\mathrm{p}} \\ \boldsymbol{\tau}_{\mathrm{m}} \end{pmatrix} + \begin{pmatrix} \boldsymbol{\tau}_{\mathrm{p,ext}} \\ \boldsymbol{\tau}_{\mathrm{m,ext}} \end{pmatrix}, \tag{28}$$

3) Kinematic stability condition (11):

$$\boldsymbol{\Sigma}(\boldsymbol{q}, \boldsymbol{\phi}_{\mathrm{ref}}) v_{\mathrm{ref}} = \dot{\boldsymbol{\xi}}_{\mathrm{des}} - \boldsymbol{\Omega}_{\mathrm{p}} \widetilde{\boldsymbol{\xi}} \tag{29}$$

$$\dot{\boldsymbol{\eta}}_{\mathrm{ref}} = \dot{\boldsymbol{\eta}}_{\mathrm{des}} - \boldsymbol{\Omega}_{\mathrm{m}} \widetilde{\boldsymbol{\eta}}\,. \tag{30}$$

First, the platform subsystem is considered. Defining the platform position error $\widetilde{\boldsymbol{\xi}} = \boldsymbol{\xi} - \boldsymbol{\xi}_{\mathrm{des}}$, from the first line of (27) with (29) follows directly the exponentially stable platform dynamics

$$\dot{\widetilde{\boldsymbol{\xi}}} = -\boldsymbol{\Omega}_{\mathrm{p}} \widetilde{\boldsymbol{\xi}}\,. \tag{31}$$

Note that the platform velocity controller compensates for external forces acting on the platform, for the dynamic couplings of the arm, as well as for the remaining platform dynamics in (28). Second, the arm subsystem is analyzed using the second line of (28), assuming free motion of the arm ($\boldsymbol{\tau}_{\mathrm{m,ext}} = \boldsymbol{0}$):

$$\boldsymbol{M}_{\mathrm{pm}}^T \dot{v}_{\mathrm{ref}} + \boldsymbol{M}_{\mathrm{m}} \ddot{\boldsymbol{\eta}} + \boldsymbol{C}_{\mathrm{mp}} v_{\mathrm{ref}} + \boldsymbol{C}_{\mathrm{m}} \dot{\boldsymbol{\eta}} + \boldsymbol{g}_{\mathrm{m}} = \boldsymbol{\tau}_{\mathrm{m}}\,. \tag{32}$$

Splitting the torque control law (10) in a similar manner results in

$$\begin{aligned} \boldsymbol{\tau}_{\mathrm{m}} =& \boldsymbol{M}_{\mathrm{pm}}^T \dot{v}_{\mathrm{ref}} + \boldsymbol{M}_{\mathrm{m}} \ddot{\boldsymbol{\eta}}_{\mathrm{ref}} + \boldsymbol{C}_{\mathrm{mp}} v_{\mathrm{ref}} \\ &+ \boldsymbol{C}_{\mathrm{m}} \dot{\boldsymbol{\eta}}_{\mathrm{ref}} + \boldsymbol{g}_{\mathrm{m}} - \boldsymbol{K}_{\mathrm{m}} \widetilde{\boldsymbol{\eta}} - \boldsymbol{H}_{\mathrm{m}} \boldsymbol{\sigma}\,, \end{aligned} \tag{33}$$

with $\widetilde{\boldsymbol{\eta}} = \boldsymbol{\eta} - \boldsymbol{\eta}_{\mathrm{des}}$ and $\boldsymbol{\sigma} = \dot{\boldsymbol{\eta}} - \dot{\boldsymbol{\eta}}_{\mathrm{ref}}$. Note that (33) contains a compensation of the inertia couplings between platform and arm. Applying (33) to (32) yields the closed-loop error dynamics of the arm

$$\boldsymbol{M}_{\mathrm{m}} \dot{\boldsymbol{\sigma}} + (\boldsymbol{C}_{\mathrm{m}} + \boldsymbol{H}_{\mathrm{m}}) \boldsymbol{\sigma} + \boldsymbol{K}_{\mathrm{m}} \widetilde{\boldsymbol{\eta}} = \boldsymbol{0}\,. \tag{34}$$

Then, uniform exponential stability of the equilibrium $(\widetilde{\boldsymbol{\eta}}^*, \dot{\widetilde{\boldsymbol{\eta}}}^*) = (\boldsymbol{0}, \boldsymbol{0})$ of (34) can be straightforwardly shown, following the same line of argumentation as in the case of platform torque control, using the positive definite Lyapunov function

$$V_\eta(\widetilde{\boldsymbol{\eta}}, \boldsymbol{\sigma}, t) = \frac{1}{2} \boldsymbol{\sigma}^T \boldsymbol{M}_{\mathrm{m}} \boldsymbol{\sigma} + \frac{1}{2} \widetilde{\boldsymbol{\eta}}^T \boldsymbol{K}_{\mathrm{m}} \widetilde{\boldsymbol{\eta}}\,. \tag{35}$$

Remark 6. Since the platform velocity controller automatically compensates for external forces acting on the platform, only free motion of the robot arm has to be assumed for the proof of stability, whereas the wheel-ground contact forces do not need to be known or compensated. On the one hand, this eliminates a source of model uncertainties (recall that a perfect compensation of wheel-ground contact forces is assumed in the torque-controlled case, which is hard to implement in practice). On the other hand, it means that the platform does not react to other interaction forces, i. e., it does not feature active compliance.

To demonstrate the effect of using platform velocity control compared to platform torque control, the results of an experimental comparison are shown in Section IV.

B. Task-space tracking controller design

In the following, the control approach is extended to the task-space tracking case. The task space is parameterized by $\boldsymbol{x}(\boldsymbol{q}) \in \mathbb{R}^m$. Then, the task velocities $\dot{\boldsymbol{x}}$ can be expressed w. r. t. the constraint-consistent velocities $\boldsymbol{v}$ using the task Jacobian matrix $\boldsymbol{J}(\boldsymbol{q}) = \partial \boldsymbol{x}(\boldsymbol{q}) / \partial \boldsymbol{q}$ as

$$\dot{\boldsymbol{x}} = \boldsymbol{J}(\boldsymbol{q}) \dot{\boldsymbol{q}} = \boldsymbol{J}(\boldsymbol{q}) \boldsymbol{S}(\boldsymbol{q}, \boldsymbol{\phi}) \boldsymbol{v}\,. \tag{36}$$

1) Control law

The control law is chosen as

$$\boldsymbol{\tau} = \boldsymbol{M} \dot{\boldsymbol{v}}_{\mathrm{ref}} + \boldsymbol{C} \boldsymbol{v}_{\mathrm{ref}} + \boldsymbol{g} - \boldsymbol{\tau}_{\mathrm{wgc}} - \boldsymbol{H} \boldsymbol{s} - \boldsymbol{S}^T \boldsymbol{J}^T \boldsymbol{K}_x \widetilde{\boldsymbol{x}} \tag{37}$$

with the constant, diagonal, p.d. matrix $\boldsymbol{K}_x \in \mathbb{R}^{m\times m}$. Using (9), (12), (36), and (37), the closed-loop error dynamics in task space are computed as

$$\dot{\widetilde{\boldsymbol{x}}} = \boldsymbol{J} \boldsymbol{S}(\boldsymbol{\phi}_{\mathrm{ref}})(\boldsymbol{s} + \boldsymbol{v}_{\mathrm{ref}}) - \dot{\boldsymbol{x}}_{\mathrm{des}}\,, \tag{38}$$

$$\boldsymbol{M} \dot{\boldsymbol{s}} + (\boldsymbol{C} + \boldsymbol{H}) \boldsymbol{s} + \boldsymbol{S}^T \boldsymbol{J}^T \boldsymbol{K}_x \widetilde{\boldsymbol{x}} = \boldsymbol{\tau}_{\mathrm{con}}\,. \tag{39}$$

The reference trajectory $(\boldsymbol{\phi}_{\mathrm{ref}}, \boldsymbol{v}_{\mathrm{ref}})$ is chosen according to the task-space kinematic stability condition

$$\boldsymbol{J}(\boldsymbol{q}) \boldsymbol{S}(\boldsymbol{q}, \boldsymbol{\phi}_{\mathrm{ref}}) \boldsymbol{v}_{\mathrm{ref}} = \dot{\boldsymbol{x}}_{\mathrm{des}} - \boldsymbol{\Omega}_x \widetilde{\boldsymbol{x}} \tag{40}$$

with the constant, diagonal, p.d. gain matrix $\boldsymbol{\Omega}_x \in \mathbb{R}^{m\times m}$.

Proposition 2.
For a non-redundant robotic system in free motion ($\boldsymbol{\tau}_{\mathrm{con}} = \boldsymbol{0}$), the equilibrium $(\widetilde{\boldsymbol{x}}^*, \boldsymbol{s}^*) = (\boldsymbol{0}, \boldsymbol{0})$ of the closed-loop equations (38)–(39) *is uniformly locally exponentially stable if the reference trajectory is chosen according to* (40).

Proof:
Choosing the Lyapunov function candidate

$$V_x(\widetilde{\boldsymbol{x}}, \boldsymbol{s}, t) = \frac{1}{2} \boldsymbol{s}^T \boldsymbol{M} \boldsymbol{s} + \frac{1}{2} \widetilde{\boldsymbol{x}}^T \boldsymbol{K}_x \widetilde{\boldsymbol{x}} \tag{41}$$

and assuming the case of free motion, i. e., $\boldsymbol{\tau}_{\mathrm{con}} = \boldsymbol{0}$, yields the time derivative

$$\dot{V}_x(\widetilde{\boldsymbol{x}}, \boldsymbol{s}, t) = -\boldsymbol{s}^T \boldsymbol{H} \boldsymbol{s} + \widetilde{\boldsymbol{x}}^T \boldsymbol{K}_x (\boldsymbol{J} \boldsymbol{S}(\boldsymbol{\phi}_{\mathrm{ref}}) \boldsymbol{v}_{\mathrm{ref}} - \dot{\boldsymbol{x}}_{\mathrm{des}})\,. \tag{42}$$

Inserting (40) into (42) results in

$$\dot{V}_x(\widetilde{\boldsymbol{x}}, \boldsymbol{s}, t) = -\boldsymbol{s}^T \boldsymbol{H} \boldsymbol{s} - \widetilde{\boldsymbol{x}}^T \boldsymbol{K}_x \boldsymbol{\Omega}_x \widetilde{\boldsymbol{x}}\,, \tag{43}$$

which is negative definite in $(\widetilde{\boldsymbol{x}}, \boldsymbol{s})$, similar to (17). If the robot is non-redundant ($m = n$), the mapping $\boldsymbol{x} = \boldsymbol{h}(\boldsymbol{q})$ is locally 1:1 and invertible. Then, (41) is positive definite for the complete state of the robot, thus it is indeed a Lyapunov function for the system (38)–(39). Proceeding analogously to Section A, it can be shown that V_x is decrescent by computing the respective time-invariant bounds for (41) and (42). Consequently, the desired task-space trajectory

$(\widetilde{\boldsymbol{x}}, \boldsymbol{s}) = (\mathbf{0}, \mathbf{0})$ can be proven to be uniformly exponentially stable. ■

Moreover, from (38) and (40) follows that

$$\dot{\widetilde{\boldsymbol{x}}} = \boldsymbol{J}\boldsymbol{S}\boldsymbol{s} - \boldsymbol{\Omega}_x \widetilde{\boldsymbol{x}}\,, \tag{44}$$

and thus $(\widetilde{\boldsymbol{x}}^*, \boldsymbol{s}^*) = (\mathbf{0}, \mathbf{0}) \rightarrow (\widetilde{\boldsymbol{x}}^*, \dot{\widetilde{\boldsymbol{x}}}^*) = (\mathbf{0}, \mathbf{0})$. Note that for task-space coordinates, stability statements can in general only be made locally (e. g. , due to task space singularities or orientation tasks defined in SO(3)).

2) Redundancy resolution

If the robot is redundant ($m < n$), (41) is only positive semi-definite and thus, no statements about stability can be made from (43). In this case, the null space of the robot has to be properly defined in order to guarantee convergence of the redundant DOF. Common possibilities to cope with the kinematic redundancy are the implementation of a task hierarchy via null-space projectors (e. g. [21], [39]–[42]), or numerical optimization strategies [43], [44]. While one of the advantages of the null-space projection lies in the strictness of the task hierarchy, the optimization-based approaches can handle both equality and inequality constraints, with possibly varying task priorities [45]. The possibility to assign a number of tasks simultaneously predestines these methods for robots with a great number of DOF and thus a high degree of redundancy. However, both approaches are computationally expensive and might thus not be applicable under the hardware restrictions of a space mission. We present an alternative solution to resolve the redundancy, which is computationally cheaper and allows a straightforward analytical proof of asymptotic stability. The method is particularly suited for systems with a small degree of redundancy, which are predominant in current space missions [2].[5]

Therefore, the robot coordinates $\boldsymbol{q}$ are split into $\boldsymbol{q}_x \in \mathbb{R}^m$ (m coordinates that are used to fulfill the task such that $\boldsymbol{x} = \boldsymbol{h}(\boldsymbol{q}_x)$ is locally 1:1 and invertible) and the remaining $\boldsymbol{q}_y \in \mathbb{R}^{(n-m)}$ coordinates, which are used to define the null space. A desired joint-space trajectory for the null space coordinates is given as $\boldsymbol{q}_{y,\mathrm{des}}(t), \dot{\boldsymbol{q}}_{y,\mathrm{des}}(t), \ddot{\boldsymbol{q}}_{y,\mathrm{des}}(t)$. Then, also the reference velocities are split:

$$\boldsymbol{v}_{\mathrm{ref}} = \begin{pmatrix} \boldsymbol{v}_{x,\mathrm{ref}} \\ \dot{\boldsymbol{q}}_{y,\mathrm{ref}} \end{pmatrix}, \tag{45}$$

and thus

$$\boldsymbol{s} = \begin{pmatrix} \boldsymbol{v} - \boldsymbol{v}_{x,\mathrm{ref}} \\ \dot{\boldsymbol{q}}_y - \dot{\boldsymbol{q}}_{y,\mathrm{ref}} \end{pmatrix}. \tag{46}$$

An additional torque input is added to the control law, which acts only on the null space coordinates:

$$\boldsymbol{\tau} = \boldsymbol{M}\dot{\boldsymbol{v}}_{\mathrm{ref}} + \boldsymbol{C}\boldsymbol{v}_{\mathrm{ref}} + \boldsymbol{g} - \boldsymbol{\tau}_{\mathrm{wgc}} - \boldsymbol{H}\boldsymbol{s} - \boldsymbol{S}^T\boldsymbol{J}^T\boldsymbol{K}_x\widetilde{\boldsymbol{x}} - \boldsymbol{\tau}_y \tag{47}$$

with

$$\boldsymbol{\tau}_y = \begin{pmatrix} \mathbf{0} \\ \boldsymbol{G}\widetilde{\boldsymbol{q}}_y \end{pmatrix} \tag{48}$$

with $\boldsymbol{G} \in \mathbb{R}^{(n-m)\times(n-m)}$ being diagonal, p.d. and constant, and $\widetilde{\boldsymbol{q}}_y = \boldsymbol{q}_y - \boldsymbol{q}_{y,\mathrm{des}}(t)$. Now, a quadratic potential for the null space coordinates is added to the Lyapunov function candidate in order to make it positive definite:

$$V_{x,y}(\boldsymbol{s}, \boldsymbol{q}, t) = \frac{1}{2}\boldsymbol{s}^T\boldsymbol{M}\boldsymbol{s} + \frac{1}{2}\widetilde{\boldsymbol{x}}^T\boldsymbol{K}_x\widetilde{\boldsymbol{x}} + \frac{1}{2}\widetilde{\boldsymbol{q}}_y^T\boldsymbol{G}\widetilde{\boldsymbol{q}}_y\,. \tag{49}$$

With $\boldsymbol{\tau}_{\mathrm{con}} = \mathbf{0}$, the time derivative becomes

$$\begin{aligned} \dot{V}_{x,y} = &- \boldsymbol{s}^T\boldsymbol{H}\boldsymbol{s} + \widetilde{\boldsymbol{x}}^T\boldsymbol{K}_x(\boldsymbol{J}\boldsymbol{S}\boldsymbol{v}_{\mathrm{ref}} - \dot{\boldsymbol{x}}_{\mathrm{des}}) \\ &- \boldsymbol{s}^T\boldsymbol{\tau}_y + \widetilde{\boldsymbol{q}}_y^T\boldsymbol{G}\dot{\widetilde{\boldsymbol{q}}}_y\,. \end{aligned} \tag{50}$$

with

$$\boldsymbol{s}^T\boldsymbol{\tau}_y = (\dot{\boldsymbol{q}}_y - \dot{\boldsymbol{q}}_{y,\mathrm{ref}})^T\boldsymbol{G}\widetilde{\boldsymbol{q}}_y\,. \tag{51}$$

In order to make the time derivative negative definite, the kinematic stability condition (40) is used again. It yields $m < n$ equations, which need to be solved for n variables. Thus, $n - m$ additional equations have to be specified to create a unique solution. These side conditions are now defined via the null-space coordinates, such that the whole $n \times n$ system of equations becomes

$$\boldsymbol{J}(\boldsymbol{q}_x, \boldsymbol{q}_y)\boldsymbol{S}(\boldsymbol{\phi}_{\mathrm{ref}})\boldsymbol{v}_{\mathrm{ref}} = \dot{\boldsymbol{x}}_{\mathrm{des}} - \boldsymbol{\Omega}_x\widetilde{\boldsymbol{x}} \tag{52}$$

$$\dot{\boldsymbol{q}}_{y,\mathrm{ref}} = \dot{\boldsymbol{q}}_{y,\mathrm{des}} - \boldsymbol{L}\widetilde{\boldsymbol{q}}_y \tag{53}$$

with $\boldsymbol{L} \in \mathbb{R}^{(n-m)\times(n-m)}$ p.d. and diagonal. This renders (50) negative definite:

$$\dot{V}_{x,y} = -\boldsymbol{s}^T\boldsymbol{H}\boldsymbol{s} - \widetilde{\boldsymbol{x}}^T\boldsymbol{K}_x\boldsymbol{\Omega}_x\widetilde{\boldsymbol{x}} - \widetilde{\boldsymbol{q}}_y^T\boldsymbol{G}\boldsymbol{L}\widetilde{\boldsymbol{q}}_y\,. \tag{54}$$

Local exponential stability of a well-defined configuration trajectory

$$\boldsymbol{q}^*(t) = \begin{pmatrix} \boldsymbol{q}_x(t) \\ \boldsymbol{q}_y(t) \end{pmatrix} = \begin{pmatrix} \boldsymbol{h}^{-1}(\boldsymbol{x}_{\mathrm{des}}(t)) \\ \boldsymbol{q}_{y,\mathrm{des}}(t) \end{pmatrix} \tag{55}$$

can be directly concluded.

C. *End of trajectory: Regulation of a static equilibrium*

In general, proofs of stability for smooth trajectory-following controllers for nonholonomic systems are only valid as long as the trajectory does not stop [47]. Therefore, time-variant or switching control laws can be utilized in order to regulate nonholonomic systems to a constant desired endpoint [48], [49]. Another approach can be found in [50], which is based on stabilizing the dynamics to a neighborhood of a given posture by modifying the system output function.

In contrast to the aforementioned approaches, we propose to switch the system characteristics artificially when the trajectory stops. This is achieved by "locking" the kinematic parameters in the close vicinity of the desired goal, creating an artificial holonomic system at the cost of losing certain DOF temporarily. For that reason, the following approach is only applicable in the case of task-space control, where the convergence to the desired endpoint can still be realized due to the inherent kinematic redundancy. In the following, $m = n - r$ is assumed, to ensure that the robot kinematics

[5]Note that the presented approach is closely related to the concept of *task augmentation* presented in [46], where the task space is augmented by kinematic functions in order to generate a quadratic and invertible task Jacobian matrix.

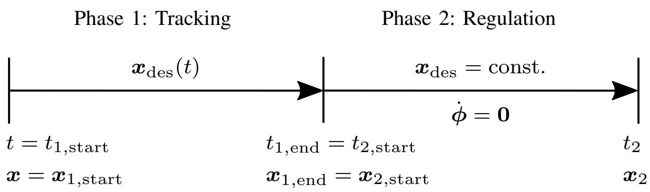

FIGURE 5: Concept of the two-phase proof of stability.

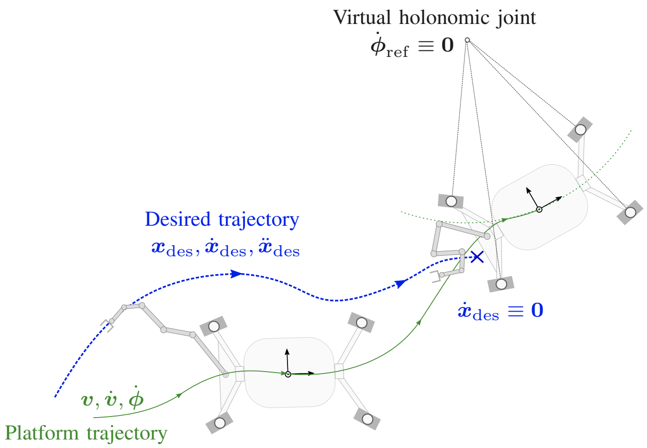

FIGURE 6: Sketch of task-space trajectory tracking. The platform trajectory is automatically derived while tracking a trajectory with the end effector. At the end of trajectory, the steering configuration is locked ($\dot{\boldsymbol{\phi}}_{\text{ref}} = \boldsymbol{0}$). In this way, a *virtual holonomic joint* is created. This turns the system into an artificially holonomic one, at the cost of losing two DOF.

is non-redundant at the end of the trajectory. Note that it is also possible to extend the following considerations $m < n - r$, e. g. by using redundancy resolution techniques as described before. The stabilization of the endpoint of a desired task-space trajectory can be achieved by the two-phase approach as depicted in Figure 5. The first phase consists of the trajectory tracking already addressed in Section III.B. The system is driven from the initial state $\boldsymbol{x}_{1,\text{start}}$ at time $t = t_{1,\text{start}}$ to a state $\boldsymbol{x}(t_{1,\text{end}}) = \boldsymbol{x}_{1,\text{end}}$. At the time when the trajectory stops, $\dot{\boldsymbol{x}}_{\text{des}} \equiv \boldsymbol{0}$. At that time, the second phase ("regulation") begins, and the terminal state of the first phase becomes the initial condition for phase two. Note that the proof of uniform exponential stability presented in Section B guarantees bounded states $\boldsymbol{x}_{1,\text{end}}$, so that the proper initialization $\boldsymbol{x}_{2,\text{start}} = \boldsymbol{x}_{1,\text{end}}$ with $t_{1,\text{end}} = t_{2,\text{start}}$ for the proof of asymptotic stability in phase 2 has already been ensured. Thereby, $\dot{\boldsymbol{\phi}}_{\text{ref}}$ is set to zero such that a holonomic system is created (with an arbitrary but static $\boldsymbol{\phi}_{\text{ref}} \equiv \overline{\boldsymbol{\phi}}_{\text{ref}}$). The idea is sketched in Figure 6.

For the regulation phase, two reasonable possibilities to choose the control law are examined in the following. The first possibility is to keep the kinematic stability condition and solve $\boldsymbol{JS}(\boldsymbol{q}, \overline{\boldsymbol{\phi}}_{\text{ref}})\boldsymbol{v}_{\text{ref}} = -\boldsymbol{\Omega}_x \widetilde{\boldsymbol{x}}$ for $\boldsymbol{v}_{\text{ref}}$ only, such that $\dot{V}_x = -\boldsymbol{sHs} - \widetilde{\boldsymbol{x}}\boldsymbol{K}_x\boldsymbol{\Omega}_x\widetilde{\boldsymbol{x}}$. This shows asymptotic stability of the origin $(\widetilde{\boldsymbol{x}}^*, \boldsymbol{s}^*) = (\boldsymbol{0}, \boldsymbol{0})$. As shown before, this implies stability of $(\widetilde{\boldsymbol{x}}^*, \dot{\widetilde{\boldsymbol{x}}}^*) = (\boldsymbol{0}, \boldsymbol{0})$. Note that switching to a static configuration $\dot{\boldsymbol{\phi}}_{\text{ref}} = \boldsymbol{0}$ reduces the number of active DOF of the artificial holonomic systems from n to $n - r$. Thus, using the redundancy resolution strategy described in Section III.B, the number of null space coordinates $\boldsymbol{q}_y$ has to be reduced such that the resulting number of equations equals $n - r$, i. e., r former null space coordinates are added to fulfill the task, and the remaining $n - r - m$ coordinates form the new null space. In particular, for $m = n - r$, no redundancy resolution has to be performed after the end of trajectory.

The second possibility is to set $\boldsymbol{v}_{\text{ref}} = \boldsymbol{0}$, yielding a classical impedance control law for the regulation phase. In this case, asymptotic convergence to the set $\mathcal{M} := \{\boldsymbol{s} = \boldsymbol{v} = \boldsymbol{0},\ \widetilde{\boldsymbol{x}} = \boldsymbol{0}\}$ can be concluded using the invariance principle of LaSalle [51]. For non-redundant systems, this implies convergence of all system states to the set $\mathcal{M}_{\text{r}} = \{\dot{\boldsymbol{q}} = \boldsymbol{0},\ \boldsymbol{q} = \boldsymbol{q}^* \mid \boldsymbol{x}(\boldsymbol{q}^*) = \boldsymbol{x}_{\text{des}}\}$. Of course, convergence of the regulation task depends on the workspace of the remaining "artificial" holonomic robot. It needs to be guaranteed that the initial state of the robot is "sufficiently close" to the desired state at the end of the trajectory. This can be supported by a) choosing a suitable trajectory, b) choosing the controller gains sufficiently high, and c) ensuring that phase 1 is long enough. In this case, the aforementioned proof of exponential stability guarantees the fulfillment of the requirement.

IV. EXPERIMENTS

The presented control approaches are validated experimentally with the LRU2, a research protoype of a planetary exloration rover built at the German Aerospace Center (DLR) according to space concept studies [52], [53]. The mobile robot is shown in Figure 1. The platform is equipped with four wheels, each with an independent steering actuator and an independent driving actuator. All wheel actuators feature RoboDrive® ILM38 BLDC drive trains with Harmonic Drive® HFUC11-100 gears, with $5\,\text{Nm}$ nominal output torque. The commercial low-level motor controllers provide the respective interfaces (position command and measurement for the steering actuators, torque or velocity command and measurement for the driving actuators), and are connected to the high-level platform controller via EtherCAT® with $1\,\text{kHz}$ cycle time. Note that no torque sensors are integrated in the drive units. Instead, scaled measurements of the motor current are used. This fact limits the performance of the low-level torque controllers. To be able to solve manipulation tasks, the rover is equipped with a 6-DOF robotic arm (Jaco2® by Kinova). The arm possesses torque sensors in each joint, the low-level joint torque controllers run in $1\,\text{kHz}$. Further technical details of the prototype can be found in [54] and [55].

In the following, three different experiments are performed. The first experiment investigates the performance of the joint-space controller using only the platform subsystem. The

TABLE 1: Gains used for the experiments. The stiffness gain $\boldsymbol{K}$ is given as a combination of the translational stiffness $\boldsymbol{K}_{\text{trans}}$ and the rotational stiffness $\boldsymbol{K}_{\text{rot}}$.

Gain	Unit	Exp. 1 (Platform only)	Exp. 2 (Tracking)	Exp. 3 (Contact)
$\boldsymbol{\Omega}_{(x)}$	$1/\text{s}$	$\text{diag}(0.1, 0.1, 0.1)$	$\text{diag}(0.7, 0.5, 0.5, 0.1, 0.1, 0.1)$	$\text{diag}(0.7, 0.5, 0.5, 0.3, 0.1, 0.1)$
$\boldsymbol{K}_{\text{trans}}$	N/m	$\text{diag}(1500, 1500)$	$\text{diag}(750, 750, 750)$	$\text{diag}(525, 525, 525)$
$\boldsymbol{K}_{\text{rot}}$	Nm/rad	150	$\text{diag}(75, 75, 75)$	$\text{diag}(52.5, 17.5, 17.5)$
$\boldsymbol{\zeta}$	–	0.5	$(0.7, 0.7, 0.7, 0.7, 0.7, 0.7)$	$(0.7, 0.7, 0.7, 0.7, 0.7, 0.7)$
$\boldsymbol{L}$	$1/\text{s}$	–	$\text{diag}(0.1, 0.1, 0.1)$	$\text{diag}(0.1, 0.1, 0.1)$
$\boldsymbol{G}$	Nm/rad	–	$\text{diag}(50, 50, 50)$	$\text{diag}(3, 3, 3)$

second and third experiment show tracking of Cartesian trajectories at the end effector. The Cartesian tracking experiments can be inspected in the accompanying video. During all experiments, the platform velocity and position are obtained from wheel odometry measurements. The position of the end effector is computed from the actual platform position combined with the forward kinematics computation of the robotic arm.

A. Modeling of the rover prototype

The nonholonomic constraint equation for the platform subsystem can be written as

$$\begin{pmatrix} -\sin(\varphi_1) & \cos(\varphi_1) & \delta_1 \\ -\sin(\varphi_2) & \cos(\varphi_2) & \delta_2 \\ -\sin(\varphi_3) & \cos(\varphi_3) & \delta_3 \\ -\sin(\varphi_4) & \cos(\varphi_4) & \delta_4 \end{pmatrix} \begin{pmatrix} {}^r v_x \\ {}^r v_y \\ \omega \end{pmatrix} = \begin{pmatrix} 0 \\ 0 \\ 0 \end{pmatrix} \tag{56}$$

with $\delta_i = l_{x,i}\cos(\varphi_i) + l_{y,i}\sin(\varphi_i)$, $i = 1, \ldots, 4$. Here, φ_i denote the steering angles of the four wheels, and $l_{x,i}, l_{y,i}$ are the distances of the i-th steering axis from the platform center in local x- and y-frames. The rover velocities (given in local r-frame) are given as ${}^r v_x$, ${}^r v_y$ (translational velocity) and ω (rotational velocity).

One possible velocity transformation $\dot{\boldsymbol{q}} = \boldsymbol{S}(\boldsymbol{\phi})v$ chosen for the following experiments is

$$\begin{pmatrix} {}^r v_x \\ {}^r v_y \\ \omega \end{pmatrix} = \begin{pmatrix} \cos\beta \\ \sin\beta \\ \kappa \end{pmatrix} v \,, \tag{57}$$

where v is the translational velocity tangential to the path of the platform. The kinematic configuration is parameterized by $\boldsymbol{\phi} = (\beta, \kappa)$, where κ denotes the curvature and β is the lateral driving angle (see Figure 3).

By choosing the steering angles according to

$$\varphi_i(\boldsymbol{\phi}) = \arctan\left(\frac{\sin\beta + l_{x,i}\kappa}{\cos\beta - l_{y,i}\kappa}\right) \,, \; i = 1, \ldots, 4, \tag{58}$$

it is ensured that $\boldsymbol{A}(\boldsymbol{\phi})\boldsymbol{S}(\boldsymbol{\phi}) = \boldsymbol{0}$ and thus the instantaneous velocity lies in the null space of the nonholonomic constraints.

B. Joint-level trajectory tracking control

The joint-level trajectory tracking experiments are performed only with the platform subsystem. The analytical solution of the kinematic stability condition (11) for this case is

$$v_{\text{ref}} = \sqrt{(v_{y,\text{des}} - q_y\tilde{y})^2 + (v_{x,\text{des}} - q_x\tilde{x})^2} \tag{59}$$

$$\kappa_{\text{ref}} = \frac{\omega_{\text{des}} - q_\theta\tilde{\theta}}{v_{\text{ref}}} \tag{60}$$

$$\beta_{\text{ref}} = \arctan\left(\frac{v_{y,\text{des}} - q_y\tilde{y}}{v_{x,\text{des}} - q_x\tilde{x}}\right) \tag{61}$$

with $(\tilde{x}, \tilde{y}, \tilde{\theta})$ denoting the coordinate errors in rover frame, and q_x, q_y, q_θ are the diagonal entries of the gain matrix $\boldsymbol{\Omega}$.[6]

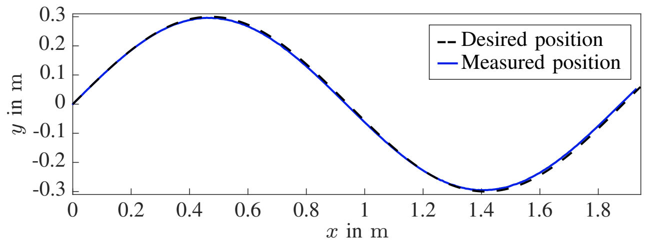

FIGURE 7: Exp. 1: Desired and measured trajectory for the mobile platform in (x, y)-coordinates.

1) Experiment 1 - Tracking a platform trajectory

A sinusoidal example trajectory in (x, y, θ) is commanded to the platform with a constant reference velocity in the x-direction of $0.05\,\text{m/s}$. The trajectory and the platform path in the x-y-plane are depicted in Figure 7. The driving experiment is performed on volcanic soil, as shown in Figure 8. In Figure 9, reference and measured position are plotted, followed by the error values for the position coordinates. The gains for the controller can be inspected in Table 1. The (scalar) damping factor H is computed w. r. t. $\boldsymbol{K}$ using the system mass of $m = 42\,\text{kg}$ and the damping ratio $\zeta = 0.5$ according to $H = 2\zeta\sqrt{\boldsymbol{S}^T\boldsymbol{K}m}$. By inspecting the upper plot of Figure 9, it can be verified that the trajectory is followed properly. The bottom plot of Figure 9 shows the tracking errors in x, y, and θ, which are in the magnitude of 1–2 cm, and $0.01\,\text{rad}$, respectively.

Table 2 shows the maximum errors and the root mean square error (RMSE) of the platform coordinates.

[6] In fact, obtaining (60)–(61) as solution for (11) requires the computation of β_{ref} using the four-quadrant inverse tangent (e. g. the Matlab `atan2` function).

TABLE 2: RMSE and maximum errors for Exp. 1.

	x	y	θ
RSME	$1.0\,\mathrm{cm}$	$0.4\,\mathrm{cm}$	$0.3°$
Max. error	$1.8\,\mathrm{cm}$	$1.3\,\mathrm{cm}$	$0.7°$

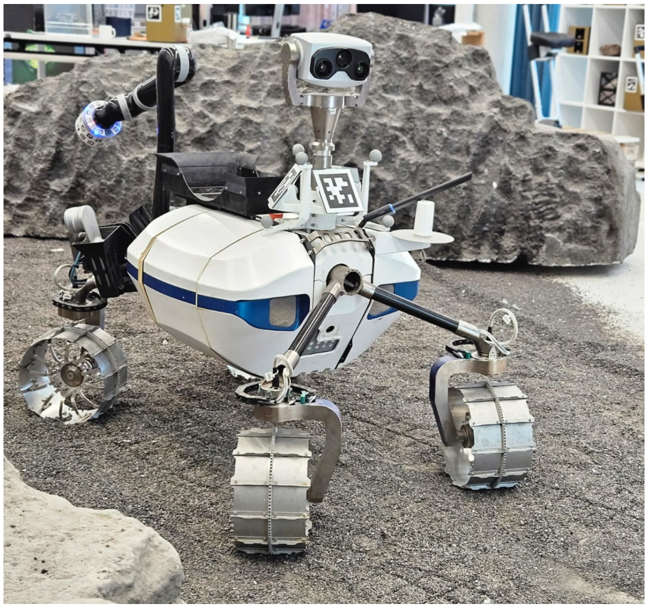

FIGURE 8: The rover driving on volcanic soil during Exp. 1.

The errors result mainly from the fact that the wheel-ground contact forces are not modeled and compensated in the experimental setting at hand, although there exist a range of methods to estimate and compensate the wheel-ground interaction forces in literature (see Section V). Thus, parts of the force transmitted through the wheels are used for soil deformation instead of platform locomotion. Note that the high-frequency oscillations in the measured errors result from oscillations in the wheel odometry measurements, which are caused by varying contact forces between wheels and ground. The dominant oscillation frequency of around $1\,\mathrm{Hz}$ hints at effects related to the wheel geometry, i. e., disturbance forces caused by the grousers, see Figure 8.

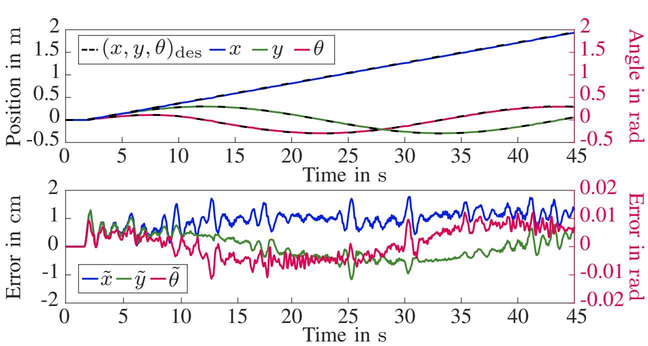

FIGURE 9: Exp. 1: Upper plot: desired and measured trajectory in (x, y, θ). Lower plot: errors in (x, y, θ) directions.

C. Cartesian trajectory tracking control

The task-level trajectory tracking experiments are performed with the complete rover, that is, including the 6-DOF arm mounted on the rover platform. A 6-DOF Cartesian trajectory is assigned to the end effector.

1) Experiment 2 - Cartesian tracking control

The goal of the second experiment is to investigate the performance of the whole-body controller using the platform torque interface compared to the platform velocity interface. Therefore, the same trajectory is commanded twice, and the results are compared pairwise. The controller gains used for Exp. 2 can be inspected in Table 1. Thereby, the damping matrix $\boldsymbol{H}$ is computed in a configuration-dependent manner using the *Double Diagonalization* approach introduced in [40]. The corresponding damping factors are given by $\boldsymbol{\zeta}$.

The desired trajectory in Cartesian coordinates of the end effector can be inspected in Figure 10. All other commanded DOF of the end effector are kept constant. Note that the command to stop the trajectory is manually triggered by the operator in this experiment. Thus, the final time and value of the trajectories vary between the datasets. During the tracking phase, the kinematic redundancy is resolved following the coordinate splitting approach described in Section 2. Thereby, the positions of the last three joints of the arm (joints number 4, 5, 6) are used as additional task coordinates $\boldsymbol{q}_y$. After the trajectory stops, only the position of joint 6 remains as nullspace condition, while joints 4 and 5 are additionally used to fulfill the main task.

In Figure 11, a 3D plot of the trajectories of both platform and end effector is shown. The initial frame is given by the position of the platform at $t = 0\,\mathrm{s}$. Figure 12 shows a comparison of the resulting tracking errors for both platform torque control in (a) and kinematic platform control (b). It can be observed that at the commanded high velocities (translational velocity of the end effector up to $0.14\,\mathrm{m/s}$), tracking errors are significant for platform torque control. Notably, the tracking performance is significantly better with kinematic platform control. To quantify the tracking performance, the RMSE for platform velocity control is computed as $2.2\,\mathrm{cm}$ for translational deviations and $4.6°$ for rotational deviations (parameterized in Euler angles). For the platform torque controller, the translational RMSE is $4.8\,\mathrm{cm}$, and the rotational RMSE is $9.9°$. The values are visualized in the bar diagram Figure 13. Thus, the total tracking error at the end effector is approximately 2.2 times larger for platform torque control than for kinematic platform control. This can be explained by the superior performance of the wheel velocity controllers compared to the wheel torque controllers.

To investigate this further, the performance of wheel velocity control versus wheel torque control is shown in Figure 14. The middle and lower plots of Figure 14 show the tracking of β_{ref} and κ_{ref}. It can be verified

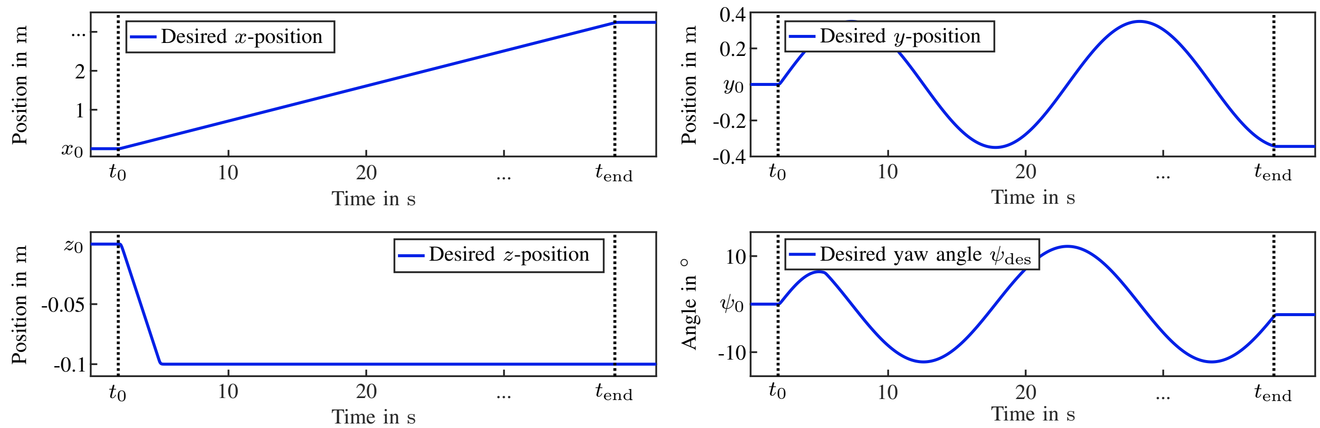

FIGURE 10: Commanded trajectory for Exp. 2, the tracking experiment. The trajectory continues periodically until the end of trajectory is commanded at t_{end}. At that time, all desired values remain constant.

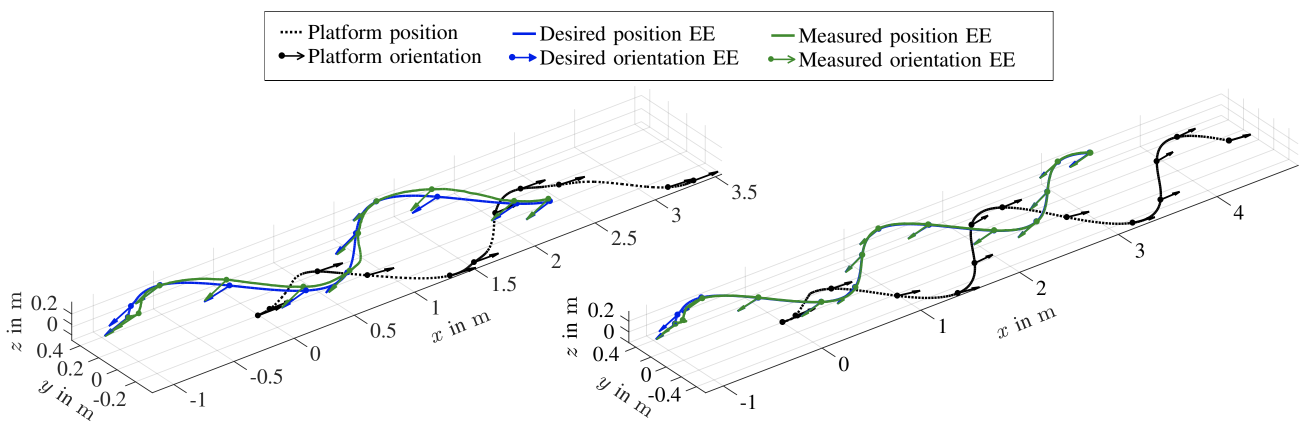

(a) Platform torque control

(b) Platform velocity control

FIGURE 11: 3D plot of the position and orientation of platform and end effector during Exp. 2.

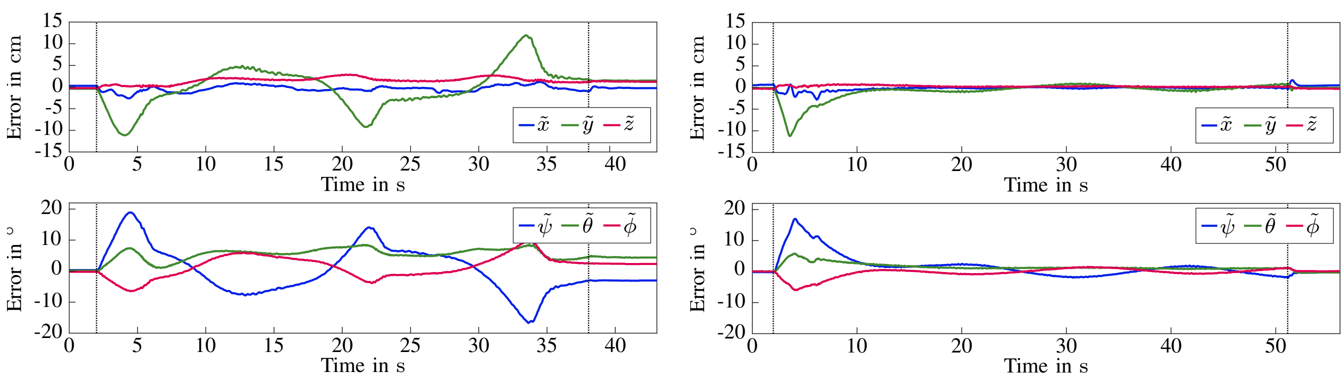

(a) Platform torque control

(b) Platform velocity control

FIGURE 12: Exp. 2: Comparison of the tracking errors for platform torque and velocity control. Upper plot: Translational errors $(\tilde{x}, \tilde{y}, \tilde{z})$. Lower plot: Rotational errors parameterized in YPR-Euler angles $(\tilde{\psi}, \tilde{\theta}, \tilde{\phi})$.

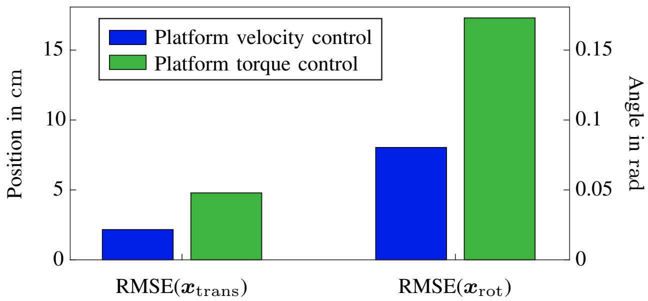

FIGURE 13: Exp. 2: Comparison of the RMSE of the end effector coordinates for platform velocity control and platform torque control.

that the underlying steering controllers follow the steering configuration properly, apart from initial reorientation effects in the first approximately $2\,\mathrm{s}$ after the start of the trajectory. The upper plot shows the tracking of the reference velocity v_{ref}. First, it can be observed that the reference velocity is limited to $0.5\,\mathrm{m/s}$. The limit is active in the first $3\,\mathrm{s}$, when the steering configuration is not yet reached and thus, no lateral velocity is created by the wheel torque or velocity controllers. Afterwards, the kinematic platform controller is able to follow the reference velocity (see Figure 14b), while the platform torque controller does produce significant tracking errors, combined with time delays of up to $2.5\,\mathrm{s}$ (cf. Figure 14a). The inferior tracking performance of the platform torque controller can again be explained by the missing compensation of wheel-ground interaction forces, as well as actuator limitations in the wheel torque controllers as described in the beginning of Section IV. In comparison to Exp. 1, the lower stiffness gain $\boldsymbol{K}_x$ causes higher tracking errors of the platform due to the aforementioned effects.

Figure 15 illustrates the effect of the platform tracking errors on the robot arm. The upper two plots show the commanded torques and the resulting joint positions for the first three arm joints. While in the case of velocity control (Figure 15b), the arm positions remain more or less constant after the initial phase (which also contains the $10\,\mathrm{cm}$ ramp in z-direction), it can be verified that the commanded joint torques for the arm partially compensate for the platform errors in Figure 15a. The effect is also visible in the video. The joint positions for joints 4 to 6 (additional task coordinates) can be inspected in the lower plot of Figure 15.

The last two seconds before the end of the trajectory are shown in detail in Figures 16 and 17. In Figure 16, one can see that the errors converge continuously after stopping the trajectory. The energy function $V_{x,y}$ from (41) is plotted in Figure 17. It is the sum of the potential energy-like part $V_{x,y,\mathrm{pot}} = \frac{1}{2}\widetilde{\boldsymbol{x}}^T\boldsymbol{K}_x\widetilde{\boldsymbol{x}}$ (plotted in blue dashed), the kinetic energy-like part $V_{x,y,\mathrm{kin}} = \frac{1}{2}\boldsymbol{s}^T\boldsymbol{M}\boldsymbol{s}$ (green dash-dotted), and the potential energy of the null space function, $V_{x,y,\mathrm{ns}} = \frac{1}{2}\widetilde{\boldsymbol{q}}_y^T\boldsymbol{G}\widetilde{\boldsymbol{q}}_y$ (yellow dash-dotted), which are also visible in the plot. Note that the null space energy jumps due to the drop of null space coordinates at $t = t_{\mathrm{end}}$. It can be verified that the sum of energies increases slightly after the end of the trajectory, and then continues converging to zero.

2) Experiment 3 - Tracking with physical contact

In the third experiment, the behavior of the controller in the presence of external disturbances is investigated. The experiment is performed with the wheel torque controller in order to demonstrate active compliance of the platform. In order to highlight the compliance of the controlled system, the stiffness gains are chosen softer than in Exp. 2, see Table 1. The end effector tracks a line trajectory with $\dot{x}_{\mathrm{des}} = -5\,\mathrm{cm/s}$, while an operator disturbs both platform and end effector manually. A series of snapshots from the experiment can be inspected in Figure 18.

It is shown that both the platform and the end effector are disturbed in different directions while the end effector follows the desired trajectory. The resulting positions of platform and end effector can be observed in Figure 19. Figure 20 shows the Euclidean norm of the translational and rotational DOF of the end effector. The snapshot pictures from Figure 18 are linked to the shown data by printing the respective letter from the caption of the sub-figures upon the plot. It can be observed that the rotational errors due to the disturbance are not converging after releasing the system at $t = 26\,\mathrm{s}$, probably due to the small gains. However, the translational errors are in the magnitude of centimeters and diminish when no external force is present. The effect of the external disturbance on the platform is visible in Figure 21, where the kinematic parameters of the platform are depicted. It can be seen that the reference values for the lateral driving angle β_{ref} and the curvature κ_{ref} change depending on the deviation of the end effector, e. g. at (a), (b), and (c), when the end effector is disturbed in different directions. The active compliance of the platform becomes visible especially in the upper plot, where the tangential velocity is depicted. At (e), the operator manually stops the platform. Therefore, the measured velocity v becomes zero. However, the arm is (partly) capable of compensating for the external disturbance by stretching out, as can be verified in Figures 20 and 18 (d)–(f).

V. DISCUSSION

The presented algorithm is motivated by a passivity-based strategy because of the particular requirements on safety and reliability demanded in robotic space missions. It is applicable to a wide variety of robotic systems, including nonholonomic wheeled mobile robots. The automatic generation of steering angles from a given trajectory makes it particularly suited for scenarios with unknown or unforeseen external disturbances, e. g. in the context of planetary exploration scenarios.

Controlling single wheels on torque level is demanding in practice. Not only the inherently unknown wheel-ground interaction forces have to be compensated, but also hardware requirements like proper torque sensors in the wheel hubs are not taken for granted in many existing platforms. On the

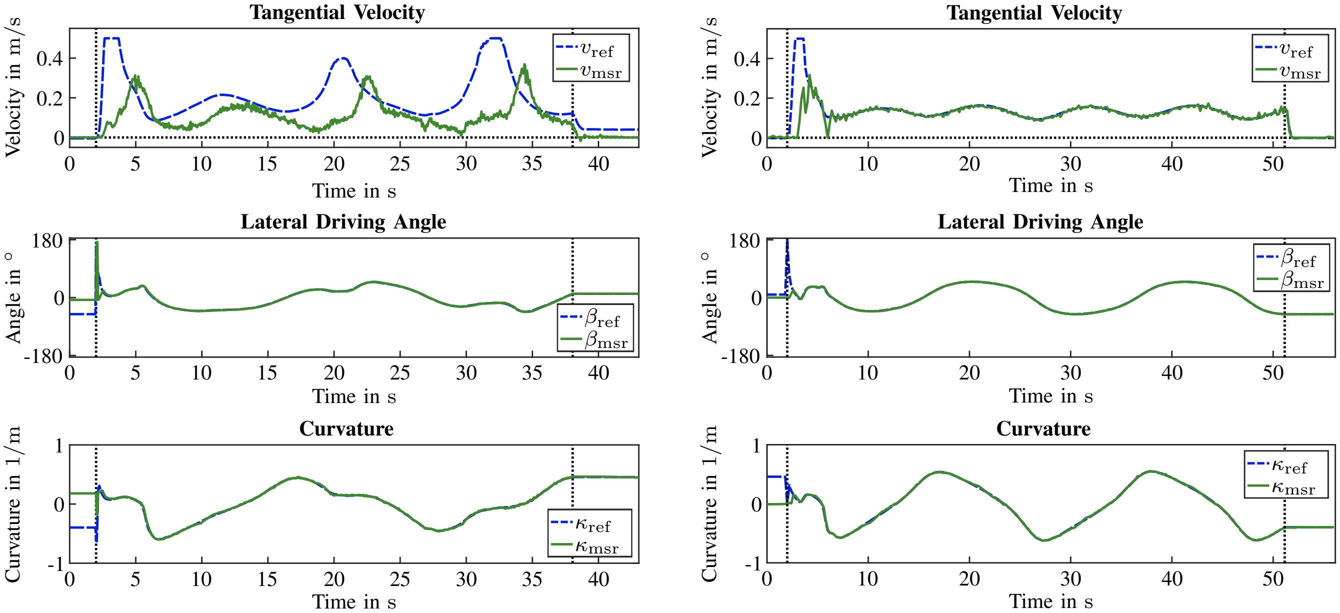

(a) Platform torque control

(b) Platform velocity control

FIGURE 14: Exp. 2: Comparison of the performance of platform torque and velocity controller while the end effector tracks a sinusoidal trajectory. Upper plot: Tracking of the reference velocity v_{ref}. Middle plot/lower plot: Tracking of the lateral driving angle β_{ref} and the reference curvature κ_{ref} with the position-controlled steering actuators.

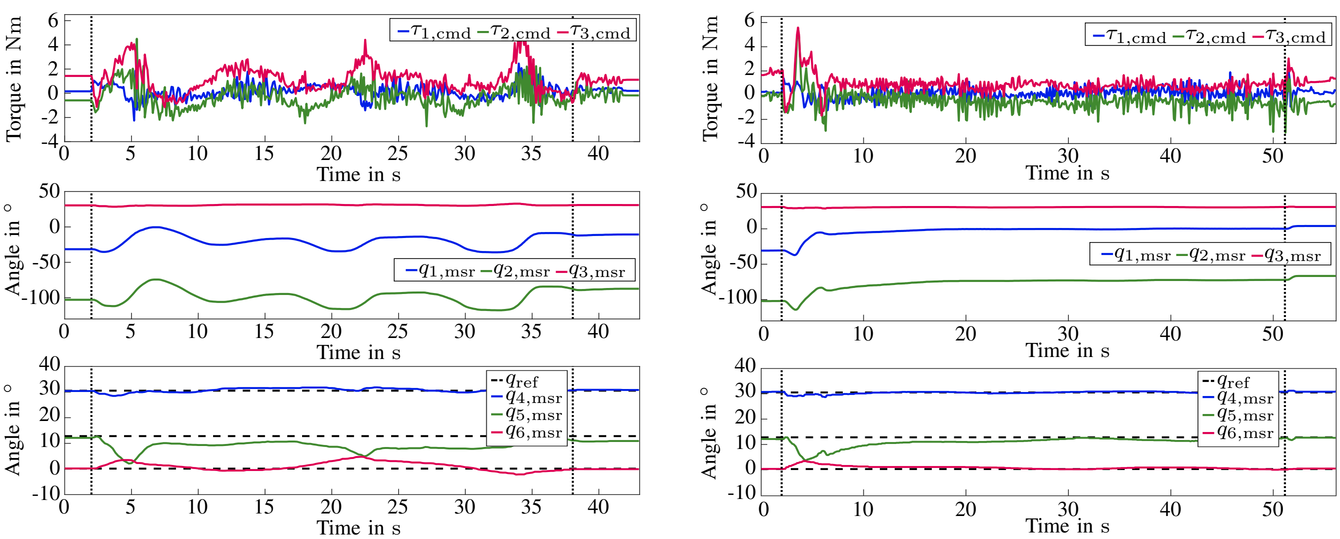

(a) Platform torque control

(b) Platform velocity control

FIGURE 15: Exp. 2: Comparison of commanded torques and measured angles for the robot arm. Upper plot: Commanded torques for joints 1, 2, 3. Center plot: Measured angles for joints 1, 2, 3. Lower plot: Reference values and measured angles for joints 4, 5, 6 (additional joint-space potential for redundancy resolution).

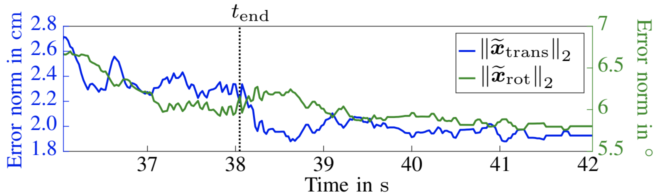

FIGURE 16: Exp. 2 (platform torque control): Euclidean norm of the translational (blue) and rotational (green) errors at the end effector. The plot shows the time span two seconds before until four seconds after the end of the trajectory.

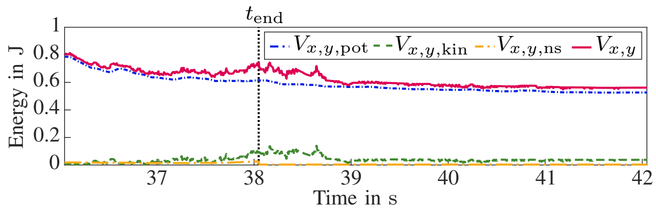

FIGURE 17: Exp. 2 (platform torque control): Energy function at the end of the trajectory. The storage function $V_{x,y}$ (magenta) is the sum of the kinetic part $V_{x,y,\text{kin}}$ (green dash-dotted), the task space potential $V_{x,y,\text{pot}}$ (blue dashed), and the additional joint space potential, $V_{x,y,\text{ns}}$ (yellow dash-dotted).

other hand, many wheeled robots feature a velocity control interface with comparatively high tracking performance. In this case, the presented algorithm can still be used, directly utilizing the platform velocity interface to generate the reference velocity from the tracking algorithm (without the need of an admittance simulation). The advantage is potentially better tracking performance by the mobile platform, while on the other hand active compliance of the platform is not achievable. Which of the properties is more desirable depends on the scenario. In the context of planetary exploration, using the platform velocity controller is certainly appropriate for tasks covering long distances, which require accurate platform locomotion. For delicate manipulation tasks in the vicinity of the target destination, platform torque control can be utilized, in order to exploit the extended workspace and the additional actuation torques created by the platform in the context of a compliant whole-body controller. The proposed regulation procedure for a stationary end point is particularly suited for these kind of local manipulation tasks.

The following assumptions have to be made for the formal proof of stability:

1) *The desired trajectory is chosen such that the kinematic parameters ϕ_{ref} and their first derivatives $\dot{\phi}_{\text{ref}}$ are bounded.*
   This assumption may limit the physical capabilities of a mobile platform. For the given platform kinematics with four individually steerable wheels, the system is physically capable to turn on the spot, but the choice of a bounded κ_{ref} does not allow this kind of motion. If instead the position of the ICR is chosen as kinematic parameter, the platform cannot move straight, as the ICR coordinates would attain infinitely large values. Still, a reasonable subset of trajectories can be implemented assuming a smart choice of kinematic parameters. However, there might still be instantaneous violations of this assumption (e. g. β can jump due to the value range of the $\arctan$ function).
2) *The low-level steering controllers are ideal.*
   The justification of the assumption $\phi \equiv \phi_{\text{ref}}$ clearly depends on the hardware design. However, it can be ensured by a careful selection of the desired trajectories w. r. t. the steering capabilities of the system at hand.
3) *The nominal wheel-ground interaction forces $\boldsymbol{\tau}_{\text{wgc}}$ can be computed from known and measured quantities.*
   The compensation of wheel-ground contact forces is only explicitly required when using the wheel torque controllers. Methods like e. g. [56]–[58] can be utilized in order to compensate for nominal friction forces between wheels and soil, either using on-board sensors or applying terramechanic models. On the other hand, observer-based disturbance rejection approaches as in [13] can be adopted. However, it has to be acknowledged that harsh terrains with strongly varying properties can reduce the accuracy of the mentioned methods locally. Indeed, the experiments were performed without a compensation of wheel-ground interaction forces, which leads to a significant deviation in the tracking performance in case of low stiffness gains of the whole-body torque control law.

Note that the fulfillment of the aforementioned assumptions depends on the specific robotic hardware, and thus is no limitation in general. On the contrary, the experiments verify that the control approach is applicable even if the hardware does not perfectly comply with the assumptions. This makes the presented control algorithm suitable for a broad range of WMMs in different scenarios.

Another important question is the usability of the proposed algorithms in a real space scenario, where the need for radiation-hardened components limits the available processor power and the signal-to-noise ratio of certain sensors (see e. g. [2]). In fact, these are two of the main reasons that advanced whole-body control methods have not been utilized in real planetary missions until now. We are well aware that we do not explicitly approach these limitations in our work – our proposed control laws require both the availability of sufficiently performant low-level torque controllers, and numerically expensive calculations such as the solution of (40). Thus, the proposed control approaches are probably not feasible on today's planetary rovers. Instead, we believe that there will be significant progress in the quality of space-qualified processors and sensors in the near future. A recent example which justifies this anticipation is NASA's

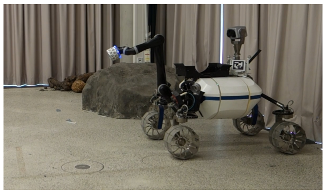

(a) $t = 2\,\mathrm{s}$
Start of trajectory.

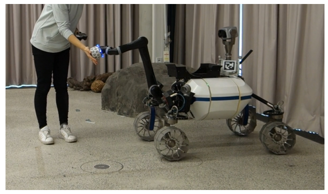

(b) $t = 8.9\,\mathrm{s}$
Contact with the end effector in x- and z-direction.

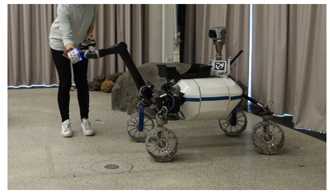

(c) $t = 13.2\,\mathrm{s}$
Pushing the end effector in negative y-direction.

(d) $t = 14.6\,\mathrm{s}$
Pulling the end effector in positive y-direction.

(e) $t = 18.7\,\mathrm{s}$
Pushing the platform in positive x-direction.

(f) $t = 21.7\,\mathrm{s}$
Pulling the platform in negative x-direction.

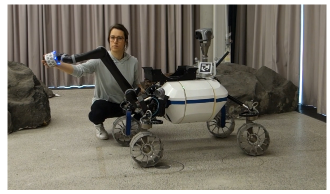

(g) $t = 24.9\,\mathrm{s}$
Disturbing the end effector.

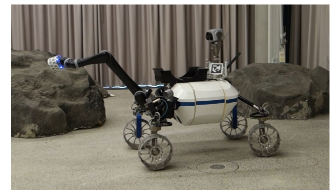

(h) $t = 32.1\,\mathrm{s}$
End of the data plotted in Figure 20 and Figure 21.

FIGURE 18: A series of snapshots from Exp. 3. The manual disturbance of both the end effector and the platform are depicted with their respective timestamps. The snapshots are linked to the corresponding data (Figure 20 and Figure 21) by the subcaptions (a)-(h).

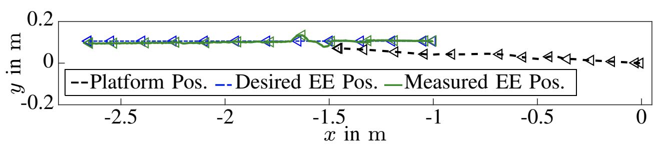

FIGURE 19: Exp. 3: Measured position of platform and end effector. Both end effector and platform are disturbed manually during the tracking phase.

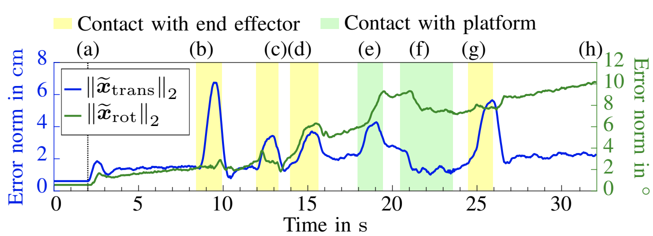

FIGURE 20: Exp. 3: Euclidean norm of translational (blue) and rotational (green) position errors at the end effector. Phases with disturbance of the end effector are highlighted in yellow, disturbance of the platform is highlighted in green. The letters (a)-(h) at the upper line of the plot correspond to the snapshots in Figure 18.

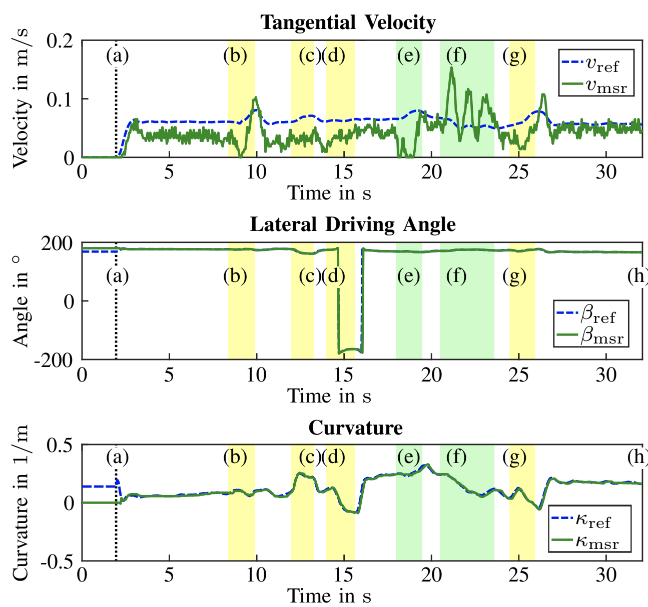

FIGURE 21: Exp. 3: Kinematic platform parameters during the contact experiment. Physical contact with the end effector is highlighted in yellow, disturbance of the platform is highlighted in green. The letters (a)–(h) correspond to the snapshots in Figure 18.

flying robot Ingenuity, which utilized a 2.26 GHz Quad-core Snapdragon™801 processor among others used to perform the expensive realtime sensor fusion and filter propagation for the use in flight control [59]. This example shows that more powerful and modern processors can already be used on Mars – provided redundancy of critical hardware components and intelligent system architecture.

VI. CONCLUSION

In this work, we presented a whole-body trajectory tracking controller for wheeled planetary rovers. The passivity-based control law computes a torque command for both the manipulator and the platform, along with a desired steering configuration, which leads to active compliance in both the arm and the platform. Thus, the presented approach allows for the close integration of impedance-based control concepts with nonholonomically constrained system dynamics. A formal proof of stability based on Lyapunov theory is complemented by various experiments on a wheeled planetary rover. This combination of both theoretical and experimental considerations and validations predestines the proposed concept for future space missions.

References

[1] A. A. Siddiqi, *Beyond Earth: A Chronicle of Deep Space Exploration, 1958-2016* (NASA SP 2018-4041), Second edition. Washington, DC: National Aeronautics and Space Administration, Office of Communications, NASA History Division, 2018.

[2] J. Bowkett et al., "Challenges in Closed-loop Compliant Motion Control for Planetary Robotics," in *Proc. of the 2024 IEEE Aerospace Conference*, Mar. 2024, pp. 1–11.

[3] A. Ellery, *Planetary Rovers: Robotic Exploration of the Solar System*. Berlin, Heidelberg: Springer Berlin Heidelberg, 2016.

[4] N. Hogan, "Impedance Control: An Approach to Manipulation: Part I - Theory, Part II - Implementation, Part III - Applications," *Journal of Dynamic Systems, Measurement, and Control*, vol. 107, pp. 1–24, Mar. 1985.

[5] J.-J. E. Slotine and W. Li, "On the Adaptive Control of Robot Manipulators," *The International Journal of Robotics Research*, vol. 6, no. 3, pp. 49–59, Sep. 1987.

[6] B. Paden and R. Panja, "Globally asymptotically stable 'PD+' controller for robot manipulators," *International Journal of Control*, vol. 47, no. 6, pp. 1697–1712, Publisher: Taylor & Francis.

[7] N. Sadegh and R. Horowitz, "Stability and Robustness Analysis of a Class of Adaptive Controllers for Robotic Manipulators," *The International Journal of Robotics Research*, vol. 9, no. 3, pp. 74–92, Jun. 1990.

[8] A. Dietrich et al., "Practical consequences of inertia shaping for interaction and tracking in robot control," *Control Engineering Practice*, vol. 114, p. 104 875, Sep. 2021.

[9] R. Ortega and M. Spong, "Adaptive Motion Control of Rigid Robots: A Tutorial," in *Proc. of the 27th IEEE Conference on Decision and Control (CDC)*, vol. 2, Dec. 1988, pp. 1575–1584.

[10] V. Rajendran et al., "Towards Autonomous Selective Harvesting: A Review of Robot Perception, Robot Design, Motion Planning and Control," *Journal of Field Robotics*, vol. 41, no. 7, pp. 2247–2279, 2024.

[11] S. Thakar et al., "A Survey of Wheeled Mobile Manipulation: A Decision-Making Perspective," *Journal of Mechanisms and Robotics*, vol. 15, no. 020801, Jul. 19, 2022.

[12] R. Holmberg and O. Khatib, "Development and control of a holonomic mobile robot for mobile manipulation tasks," *International Journal of Robotics Research*, vol. 19, no. 11, pp. 1066–1074, 2000.

[13] C. Ren, Y. Ding, and S. Ma, "Passivity-Based Active Disturbance Rejection Control of an Omnidirectional Mobile Robot," in *2018 IEEE 8th Annual International Conference on CYBER Technology in Automation, Control, and Intelligent Systems (CYBER)*, Jul. 2018, pp. 1513–1518.

[14] G. D. White, R. M. Bhatt, and V. N. Krovi, "Dynamic redundancy resolution in a nonholonomic wheeled mobile manipulator," *Robotica*, vol. 25, no. 2, pp. 147–156, Mar. 2007.

[15] G. D. White, R. M. Bhatt, C. P. Tang, and V. N. Krovi, "Experimental Evaluation of Dynamic Redundancy Resolution in a Nonholonomic Wheeled Mobile Manipulator," *IEEE/ASME Transactions on Mechatronics*, vol. 14, no. 3, pp. 349–357, Jun. 2009.

[16] K. Xia et al., "Trajectory Tracking Control of Wheeled Mobile Manipulator Based on Fuzzy Neural Network and Extended Kalman Filtering," *Neural Computing and Applications*, vol. 30, no. 2, pp. 447–462, Jul. 2018.

[17] W. Yuan, Y.-H. Liu, C.-Y. Su, and F. Zhao, "Whole-body control of an autonomous mobile manipulator using model predictive control and adaptive fuzzy technique," *IEEE Transactions on Fuzzy Systems*, vol. 31, no. 3, pp. 799–809, 2023.

[18] Y. Wang, R. Chen, and M. Zhao, "Whole-Body Model Predictive Control for Mobile Manipulation With Task Priority Transition," in *Proc. of the 2025 IEEE International Conference on Robotics and Automation*, 2025, pp. 13 356–13 362.

[19] Y. Umeda, D. Nakamura, T. Murakami, and K. Ohnishi, "Hybrid Position/Force Control of a Mobile Manipulator Based on Cooperative Task Sharing," in *Proc. of the IEEE International Symposium on Industrial Electronics ISIE '99.*, vol. 1, Jul. 1999, pp. 139–144.

[20] D. Omrčen, L. Žlajpah, and B. Nemec, "Autonomous motion of a mobile manipulator using a combined torque and velocity control," *Robotica*, vol. 22, no. 6, pp. 623–632, Nov. 2004.

[21] A. Dietrich and C. Ott, "Hierarchical impedance-based tracking control of kinematically redundant robots," *IEEE Transactions on Robotics*, vol. 36, no. 1, pp. 204–221, 2020.

[22] Y. Wu, E. Lamon, F. Zhao, W. Kim, and A. Ajoudani, "Unified Approach for Hybrid Motion Control of

MOCA Based on Weighted Whole-Body Cartesian Impedance Formulation," *IEEE Robotics and Automation Letters*, vol. 6, no. 2, pp. 3505–3512, Apr. 2021.

[23] X. Wu, A. Albu-Schäffer, and A. Dietrich, "Singularity-Robust Prioritized Whole-Body Tracking and Interaction Control With Smooth Task Transitions," in *Proc. of the 2024 IEEE International Conference on Robotics and Automation (ICRA)*, May 2024, pp. 15 358–15 365.

[24] A. Dietrich et al., "Whole-body impedance control of wheeled mobile manipulators: Stability analysis and experiments on the humanoid robot Rollin' Justin," *Autonomous Robots (AURO): Special Issue on Whole-Body Control of Contacts and Dynamics for Humanoid Robots*, vol. 40, no. 3, pp. 505–517, Mar. 2016.

[25] S. Djebrani, A. Benali, and F. Abdessemed, "Modelling and control of an omnidirectional mobile manipulator," en, *International Journal of Applied Mathematics and Computer Science*, vol. 22, no. 3, pp. 601–616, Sep. 2012.

[26] M. J. Schuster et al., "The ARCHES Space-Analogue Demonstration Mission: Towards Heterogeneous Teams of Autonomous Robots for Collaborative Scientific Sampling in Planetary Exploration," *IEEE Robotics and Automation Letters*, vol. 5, no. 4, pp. 5315–5322, 2020.

[27] A. Wedler et al., "Finally! Insights into the ARCHES Lunar Planetary Exploration Analogue Campaign on Etna in summer 2022," in *73rd International Astronautical Congress, IAC 2022*, Paris, France, Sep. 2022.

[28] V. Padois, J.-Y. Fourquet, and P. Chiron, "Kinematic and dynamic model-based control of wheeled mobile manipulators: A unified framework for reactive approaches," *Robotica*, vol. 25, no. 2, pp. 157–173, Mar. 2007.

[29] G. Campion and W. Chung, "Wheeled Robots," in *Springer Handbook of Robotics*, B. Siciliano and O. Khatib, Eds., Berlin, Heidelberg: Springer, 2008, pp. 391–410.

[30] G. Campion, G. Bastin, and B. D'Andréa-Novel, "Structural Properties and Classification of Kinematic and Dynamic Models of Wheeled Mobile Robots," *IEEE Transactions on Robotics and Automation*, vol. 12, no. 1, pp. 47–62, 1996.

[31] F. Ghorbel, B. Srinivasan, and M. W. Spong, "On the uniform boundedness of the inertia matrix of serial robot manipulators," *Journal of Robotic Systems*, vol. 15, no. 1, pp. 17–28, 1998.

[32] R. M. Murray, Z. Li, and S. S. Sastry, *A Mathematical Introduction to Robotic Manipulation*. CRC Press, 1994.

[33] C. P. Connette, A. Pott, M. Hägele, and A. Verl, "Control of an Pseudo-omnidirectional, Non-holonomic, Mobile Robot based on an ICM Representation in Spherical Coordinates," in *Proc. of the 47th IEEE Conference on Decision and Control*, Dec. 2008, pp. 4976–4983.

[34] L. Le Tien, A. Albu-Schaffer, A. De Luca, and G. Hirzinger, "Friction Observer and Compensation for Control of Robots with Joint Torque Measurement," in *2008 IEEE/RSJ International Conference on Intelligent Robots and Systems*, Nice: IEEE, Sep. 2008, pp. 3789–3795.

[35] R. Courant, "Über die Eigenwerte bei den Differentialgleichungen der mathematischen Physik," *Mathematische Zeitschrift*, vol. 7, no. 1, pp. 1–57, Mar. 1920.

[36] E. Fischer, "Über quadratische Formen mit reellen Koeffizienten," *Monatshefte für Mathematik und Physik*, vol. 16, no. 1, pp. 234–249, Dec. 1905.

[37] H. K. Khalil, *Nonlinear Systems*, 3. ed. Upper Saddle River, NJ: Prentice Hall, 2002.

[38] K. Lakatos, D. Lakatos, X. Wu, P. Kotyczka, and A. Dietrich, "On passivity-based trajectory tracking for robotic manipulators combining PD+ and Slotine-Li control," *at - Automatisierungstechnik*, vol. 72, no. 12, pp. 1195–1206, Dec. 2024.

[39] O. Khatib, "A Unified Approach for Motion and Force Control of Robot Manipulators: The Operational Space Formulation," *IEEE Journal of Robotics and Automation*, vol. RA-3, no. 1, pp. 43–53, Feb. 1987.

[40] A. Albu-Schäffer, C. Ott, U. Frese, and G. Hirzinger, "Cartesian Impedance Control of Redundant Robots: Recent Results with the DLR-Light-Weight-Arms," in *Proc. of the 2003 IEEE International Conference on Robotics and Automation*, vol. 3, Taipei, Taiwan: IEEE, Sep. 2003, pp. 3704–3709.

[41] A. Dietrich, C. Ott, and A. Albu-Schäffer, "An overview of null space projections for redundant, torque-controlled robots," *The International Journal of Robotics Research*, vol. 34, no. 11, pp. 1385–1400, Sep. 2015.

[42] X. Wu, C. Ott, A. Albu-Schäffer, and A. Dietrich, "Passive Decoupled Multitask Controller for Redundant Robots," *IEEE Transactions on Control Systems Technology*, vol. 31, no. 1, pp. 1–16, Jan. 2023.

[43] O. Kanoun, F. Lamiraux, and P.-B. Wieber, "Kinematic Control of Redundant Manipulators: Generalizing the Task-Priority Framework to Inequality Task," *IEEE Transactions on Robotics*, vol. 27, no. 4, pp. 785–792, Aug. 2011.

[44] A. Escande, N. Mansard, and P.-B. Wieber, "Hierarchical Quadratic Programming: Fast Online Humanoid-Robot Motion Generation," *The International Journal of Robotics Research*, vol. 33, no. 7, pp. 1006–1028, Jun. 2014.

[45] S. Kim et al., "Whole-body Control of Non-holonomic Mobile Manipulator Based on Hierarchical Quadratic Programming and Continuous Task Transition," in *2019 IEEE 4th International Conference on Ad-*

vanced Robotics and Mechatronics (ICARM), Jul. 2019, pp. 414–419.

[46] H. Seraji, "Configuration control of redundant manipulators: Theory and implementation," *IEEE Transactions on Robotics and Automation*, vol. 5, no. 4, pp. 472–490, 1989.

[47] R. W. Brockett et al., "Asymptotic stability and feedback stabilization," *Differential geometric control theory*, vol. 27, no. 1, pp. 181–191, 1983.

[48] B. Thuilot, B. d'Andréa-Novel, and A. Micaelli, "Modeling and feedback control of mobile robots equipped with several steering wheels," *IEEE Transactions on Robotics and Automation*, vol. 12, no. 3, pp. 375–390, Jun. 1996.

[49] G. Oriolo, A. De Luca, and M. Vendittelli, "WMR control via dynamic feedback linearization: Design, implementation, and experimental validation," *IEEE Transactions on Control Systems Technology*, vol. 10, no. 6, pp. 835–852, Nov. 2002.

[50] C. Gruber and M. Hofbaur, "Practically stabilizing motion control of mobile robots with steering wheels," in *Proc. of the 2014 IEEE Conference on Control Applications (CCA)*, Oct. 2014, pp. 1312–1317.

[51] J. P. LaSalle, "Stability Theory for Ordinary Differential Equations," *Journal of Differential Equations*, vol. 4, no. 1, pp. 57–65, Jan. 1968.

[52] M. J. Schuster et al., "The LRU Rover for Autonomous Planetary Exploration and Its Success in the SpaceBotCamp Challenge," in *2016 International Conference on Autonomous Robot Systems and Competitions (ICARSC)*, Bragança, Portugal: IEEE, May 2016, pp. 7–14.

[53] R. Haarmann, Q. Mühlbauer, L. Richter, et al., "Mobile Payload Element (MPE): Concept study of a small, autonomous and innovative sample fetching rover," in *Proc. of the 12th Symposium on Advanced Space Technologies in Robotics and Automation (ASTRA)*, 2013.

[54] A. Wedler et al., "LRU-lightweight rover unit," in *Proc. of the 13th Symposium on Advanced Space Technologies in Robotics and Automation (ASTRA)*, 2015.

[55] M. J. Schuster et al., "Towards Autonomous Planetary Exploration: The Lightweight Rover Unit (LRU), its Success in the SpaceBotCamp Challenge, and Beyond," *Journal of Intelligent & Robotic Systems (JINT)*, vol. 93, no. 3-4, pp. 461–494, Nov. 2019.

[56] K. Iagnemma and S. Dubowsky, "Traction Control of Wheeled Robotic Vehicles in Rough Terrain with Application to Planetary Rovers," *The International Journal of Robotics Research*, vol. 23, no. 10-11, pp. 1029–1040, Oct. 2004.

[57] G. Ishigami, A. Miwa, K. Nagatani, and K. Yoshida, "Terramechanics-Based Model for Steering Maneuver of Planetary Exploration Rovers on Loose Soil," *Journal of Field Robotics*, vol. 24, no. 3, pp. 233–250, 2007.

[58] L. Ding et al., "Interaction Mechanics Model for Rigid Driving Wheels of Planetary Rovers Moving on Sandy Terrain with Consideration of Multiple Physical Effects," *Journal of Field Robotics*, vol. 32, no. 6, pp. 827–859, 2015.

[59] B. Balaram et al., "Mars Helicopter Technology Demonstrator," in *Proc. of the 2018 AIAA Atmospheric Flight Mechanics Conference*, Kissimmee, Florida: American Institute of Aeronautics and Astronautics, Jan. 2018.